

# Differential erosion of a Mesozoic rift flank: Establishing the source of topography across Karrat, central West Greenland

Scott Jess<sup>a,\*</sup>, Randell Stephenson<sup>a</sup>, David H. Roberts<sup>b</sup>, Roderick Brown<sup>c</sup>

<sup>a</sup> School of Geosciences, University of Aberdeen, Aberdeen AB24 3UE, UK

<sup>b</sup> Department of Geography, Durham University, Science Laboratories, Durham DH1 3LE, UK

<sup>c</sup> School of Geographical and Earth Sciences, University of Glasgow, Glasgow G12 8QQ, UK

## ARTICLE INFO

### Article history:

Received 7 November 2018

Received in revised form 19 February 2019

Accepted 19 February 2019

Available online 4 March 2019

### Keywords:

Thermochronology

Geomorphology

Rifting

Isostasy

Greenland

## ABSTRACT

The landscape of the Karrat region, central West Greenland, contrasts between high elevation low relief topography, steep sided fjords and deep bathymetric troughs. The mechanisms controlling its formation are highly debated, with initial work suggesting it to be the result of episodic tectonic uplift throughout the late Cenozoic and alternative models implying it is the product of more recent isostatic uplift in response to differential glacial erosion. Here the results of a comprehensive low temperature thermochronological study (apatite fission track and apatite (U—Th)/He) and landscape evolution model are presented that helps establish the source of the modern elevated landscape and the region's complex geomorphology. Joint modelling of the apatite fission track and apatite (U—Th)/He data outlines two significant periods of cooling, in the Mesozoic and Cenozoic respectively. The first (150 Ma – 110 Ma) correlates to the onset of extension between West Greenland and eastern Canada, suggesting uplift of the region during active rifting, while the second period (50 Ma – 0 Ma) is coeval to the cessation of volcanism in the region and likely represents widespread erosion. These results suggest the basement escarpment likely remained at height during extrusive volcanism and was later uncovered following exhumation of the volcanic succession. Moreover, this latter phase of exhumation is outlined in the results of landscape evolution modelling, implying it likely encompassed localised differential erosion of the volcanic pile, producing a pre-glacial landscape that later aided ice stream onset and the advance of the Uummannaq Ice Stream. Glacial exhumation of the region was likely characterised by differential erosion, shaping the modern geomorphology through preferential ice stream development and isostatic rebound. These results highlight the complex interaction between rift tectonics and surface processes across the Karrat region and adds to a wider understanding of the post-rift evolution of passive continental margins.

© 2019 The Authors. Published by Elsevier B.V. This is an open access article under the CC BY license (<http://creativecommons.org/licenses/by/4.0/>).

## 1. Introduction

The elevated topography of glaciated Atlantic passive margins continues to stimulate considerable debate and discussion across the geological community (e.g., Rohrman et al., 1996; Hansen, 1996; Riis, 1996; Japsen and Chalmers, 2000; Japsen et al., 2005; Anell et al., 2009; Eidvin et al., 2014). Several continental margins exhibit low relief high elevation topography surrounded by low lying plains, deep bathymetry or sedimentary basins, believed to have formed through either episodic post-rift uplift (Green, 1989; Redfield et al., 2005; Japsen et al., 2006; Bonow et al., 2014; Japsen et al., 2014; Redfield and Osmundsen, 2014; Green et al., 2018) or a combination of pre-rift topography, rift flank uplift and denudational isostasy (Hendriks and Andriessen, 2002; Medvedev et al., 2008; Nielsen et al., 2009; Medvedev et al., 2013; Medvedev and Hartz, 2015; Egholm et al.,

2017). Diverse approaches have been utilised in attempts to better constrain the extent and timing of passive margin uplift across the Atlantic (Hansen, 1996; Riis, 1996; Rohrman et al., 1996; Japsen, 1998; Nielsen et al., 2009; Gołędowski et al., 2013; Pedersen et al., 2016), though a definitive consensus is yet to be agreed upon.

The landscape of the Nuussuaq Basin, central West Greenland, is heavily glaciated and includes elevated topography ( $\leq 2$  km) believed to have formed through either widespread differential erosion (Medvedev et al., 2013; Jess et al., 2018) or late Cenozoic episodic uplift (Bonow et al., 2006; Japsen et al., 2006). Peneplains within the landscape have previously been suggested to outline three periods of tectonic uplift between 36 Ma – 2 Ma and totalling ~3 km (Bonow et al., 2014; Japsen et al., 2006), supported by thermal history modelling and offshore unconformities (Japsen and Chalmers, 2000; Chalmers, 2000). These conclusions have been criticised previously, with Redfield (2010) concluding uncertainties within the wider thermochronological dataset could not define late Cenozoic uplift, while Jess et al. (2018) questioned both the modelling approach and interpretation of peneplains in the

\* Corresponding author.

E-mail address: [scott.jess@ucalgary.ca](mailto:scott.jess@ucalgary.ca) (S. Jess).

landscape. Furthermore, Medvedev et al. (2013) and Jess et al. (2018) proposed the basin's elevated topography may instead be the result of lengthy widespread exhumation, instigating significant positive feedback from the lithosphere and preserving much of the older topography under cold-based ice during glaciation (Strunk et al., 2017). This alternative interpretation of basin evolution appears to suit much of the data and geology in the Nuussuaq Basin better, though the cause of topography and the complex geomorphology across the surrounding basement margins remains unclear.

The present work focuses on the elevated basement margin to the NE of the Nuussuaq Basin (Fig. 1), which exhibits both high elevation low relief topography (>2 km) and deep bathymetric troughs (0.6 km) (Fig. 2). The application of both a high-density elevation profile of apatite fission track and apatite (U—Th)/He data and landscape evolution modelling are utilised to establish the timing of topographic generation across the basement margin and infer the key factors that helped shape the geomorphology. Collectively, the results aid in establishing a conceptual model that outlines how the interaction of rift tectonics, volcanism and differential exhumation combine to generate the modern landscape.

## 2. Geological and geomorphological setting

### 2.1. Geology

The geology of the study area has an Archaean-Proterozoic metamorphic basement overlain by Mesozoic sediments of the Nuussuaq Basin and Cenozoic volcanics of the West Greenland Igneous Province.

The basement rocks of the Karrat region are part of the wider Rinkian Fold Belt that formed in the Paleoproterozoic during the Trans-Hudson Orogeny (~1.87 Ga) (Sidgren et al., 2006; St-Onge et al., 2009). The principal basement units consist of the Archaean Umanak and Tasiussaq gneisses and the metasediments of the Karrat Group, a Paleoproterozoic clastic passive margin sequence that formed atop the Archaean gneisses (Grocott and McCaffrey, 2017). Following the Trans-Hudson orogeny, the region is thought to have remained at the

cratonic heart of Laurentia, though much of the observable geological record was since eroded away as a result of Mesozoic-Cenozoic rifting and widespread glaciation. Isolated sedimentary accumulations and low temperature thermochronological data from across the Slave Craton, northern Canada, suggest much of the region may have experienced subsidence and uplift during the Palaeozoic (Flowers et al., 2012; Ault et al., 2013; Pinet et al., 2013), though the lack of further geological evidence renders this interpretation contentious.

Rifting between Greenland and Canada is believed to have commenced as early as the Late Triassic (Larsen et al., 2009), subsequently forming the Nuussuaq Basin within central West Greenland during the Early Cretaceous (Dam et al., 2009). The documented clastic stratigraphy within the basin spans the Mid-Cretaceous to Early Palaeocene, detailing two periods of active rifting (Mid-Cretaceous; Late Cretaceous/Early Palaeocene) and the presence of a major deltaic system prograding from the SE (Dam et al., 2009). Within the Karrat region, only the coastal/terrestrial sands of the Upper Naes Formation are observable on the islands of Upernivik Ø and Qeqertarsuq, while the deep marine muds of the Itilli Formation are interpreted to underlie the offshore (Dam et al., 1998a). The end of clastic deposition occurs in the Early Palaeocene, as canyon and valley fill sequences outline a significant period of uplift and subsidence within the basin, prior to the onset of widespread Cenozoic volcanism (Dam et al., 1998b).

The extrusion of lavas from the West Greenland Igneous Province spanned much of the Palaeocene and Eocene, eventually covering an area of 50,000 km<sup>2</sup> (Storey et al., 1998). Lavas were sourced from multiple volcanic centres across the margin and now overlie much of the Nuussuaq Basin and offshore domain (Larsen et al., 2016) (Fig. 1). Small outcrops are found atop the region's highest topography, implying lavas covered the region during the Palaeogene (Larsen et al., 2016) (Fig. 1), whilst elevated marine, terrestrial and lacustrine syn-volcanic sediments (~1100 m) are observed throughout the southern portion of the basin indicating the extent of uplift in the region following the Palaeocene (Piasecki et al., 1992). Widespread extrusive volcanism continued until its cessation ~54 Ma, though localised lava deposits and intrusions continued until ~38 Ma, marking the end of the onshore geological record (Larsen et al., 2016).

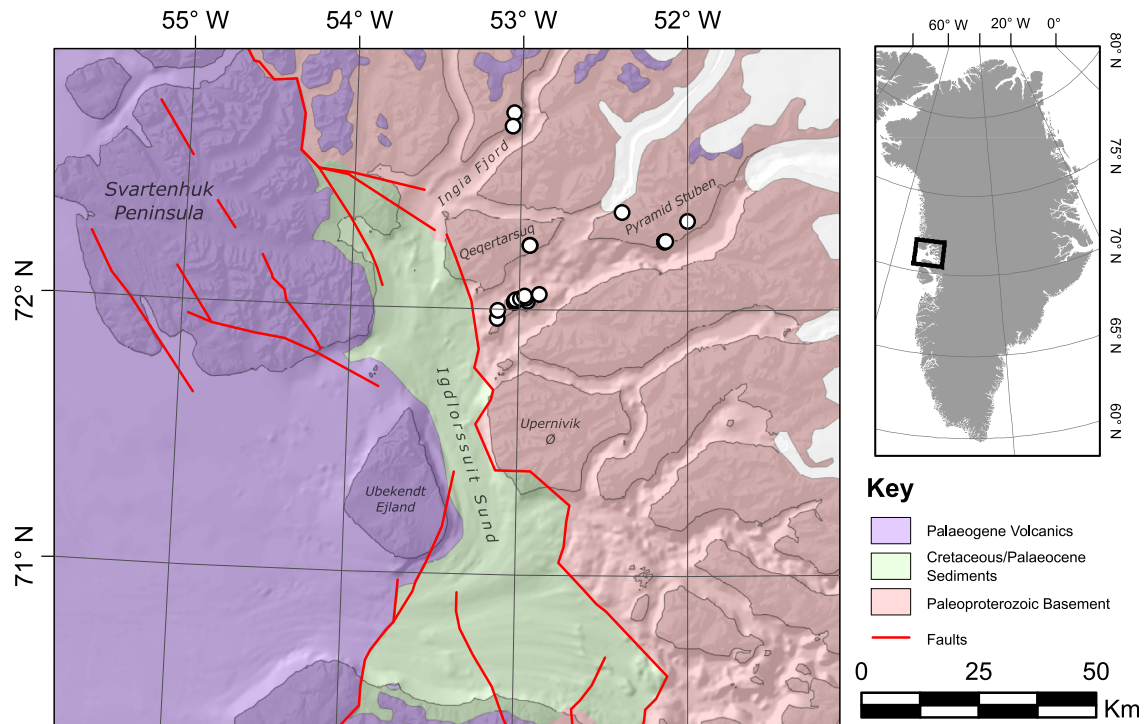


**Fig. 1.** Simplified geological map of the Karrat region displaying the sample locations (white circles) and the regions location on West Greenland (modified from Pedersen et al., 2014). The geology of the region is made up of three principal sections; Proterozoic basement to the east, Cretaceous sediments in the centre and Palaeogene volcanics to the west. The basement topography map of Greenland highlights the key topographic regions of Greenland, with the anomalous topography of the Karrat region along the western margin.

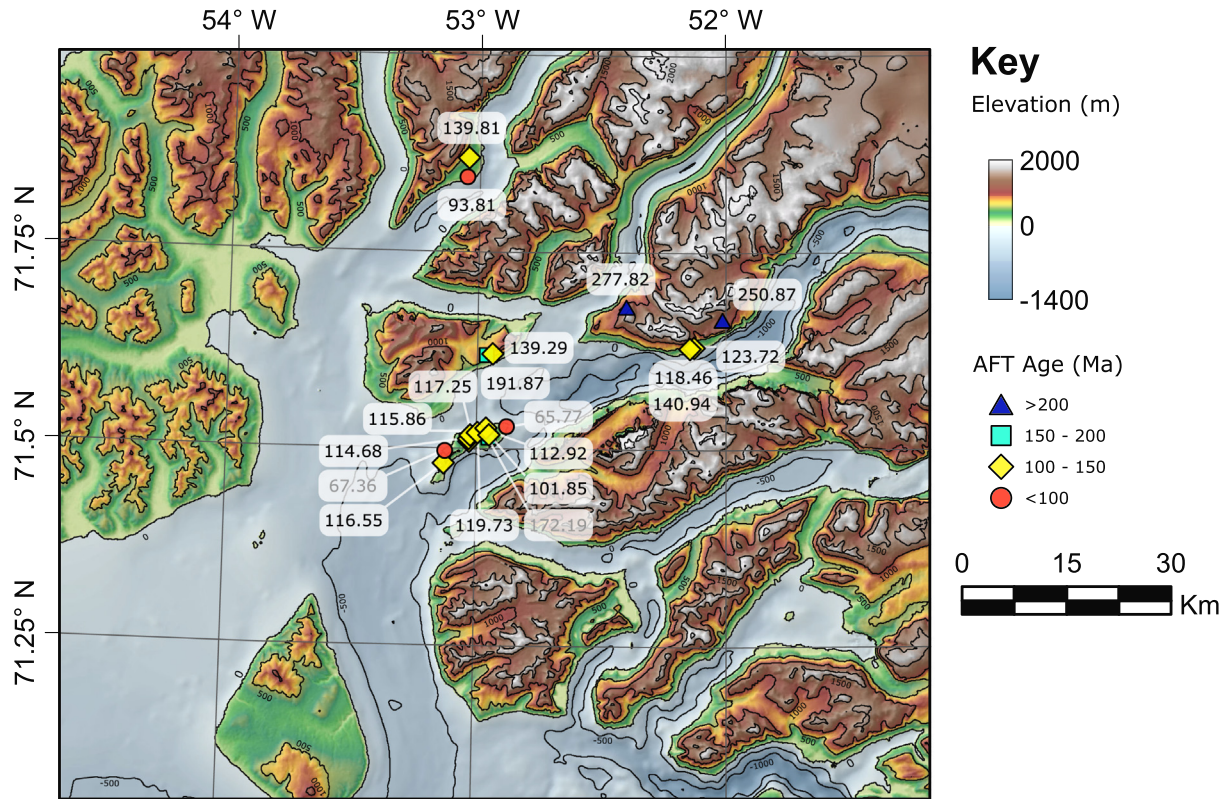


**Fig. 2.** Digital Elevation Model of the Karrat region showing sample locations and AFT ages from elevated topography (contours are spaced 500 m apart). Major geomorphological characteristics of the region include high elevated topography incised by deep fjords to the east, a low bathymetric trough in the centre of the region and elevated bathymetry and topography to the west. AFT ages range between 65 Ma – 278 Ma, though the three ages (grey) are believed to have been locally reheated and thermally reset during volcanism, rendering them unusable within this study. The DEM used is the Bedmachine v3 from [Morigheim et al. \(2017\)](#).

## 2.2. Geomorphology

The modern geomorphology of the Karrat region is characterised by high elevation basement topography, thin, steep sided fjords and a deep bathymetric trough underlying Igdlorssuit Sund (Fig. 2). This complex geomorphology has been predominantly shaped by selective linear erosion and ice stream onset in the region, as multiple fjord glaciers converged and flowed south then west onto the continental shelf as the Ummannaq Ice Stream (UIS). The underlying geology of the region and pre-glacial landscape have been cited as possible controls on the ice stream's development, restricting outlet glacier flow pathways and forcing them to coalesce and coverage, forming the UIS ([Roberts et al., 2013](#); [Lane et al., 2014](#)). The geology and geomorphology appear inherently linked, with the muds and sands of the Itilli Formation underlying the deep bathymetry of Igdlorssuit Sund and basalts and gneisses underlying the higher topography of Ubekendt Ejland and the basin margin (Fig. 1). This correlation implies the underlying geology may have been a primary control on the topographic evolution of the region, conceivably providing additional insight into the regional landscape evolution.

## 3. Methodology

### 3.1. Apatite low temperature thermochronology

This study utilises apatite fission track (AFT) and apatite (U—Th)/He (AHe) thermochronology to determine the thermal history of the region and the timing of uplift along the basement margin. AFT dating is predicated on the fission decay of  $^{238}\text{U}$  that produces linear damage trails within the apatite crystal lattice (spontaneous fission tracks). These tracks represent the extent of fission decay, while a second set of tracks, generated following irradiation of a grain, signifies the remaining

radioactive isotope concentration. The comparative densities of both sets of tracks are used to calculate a thermochronological age, while the distribution of confined track lengths assists in defining the style of cooling through the partial annealing zone (PAZ; 120 °C – 60 °C) ([Gallagher et al., 1998](#)). Details of sample preparation can be found in the supplementary data, while track densities, track lengths and Dpar (kinetic annealing parameter; [Carlson et al., 1999](#)) were measured on a Zeiss HAL 100 microscope employing FTstage software ([Dumitru, 1993](#)) at the University of Glasgow.

AHe dating utilises the diffusion and retention of  $^4\text{He}$  in apatite from the alpha decay of  $^{238}\text{U}$ ,  $^{235}\text{U}$  and  $^{232}\text{Th}$  ([Zeitler et al., 1987](#)). Temperature sensitivity of the system varies within the partial retention zone (HePRZ; 70 °C – 40 °C) dependent on the thermal history ([Stockli et al., 2000](#)), grain geometry ([Farley, 2000](#)) and effect of radiation damage ([Shuster et al., 2006](#); [Flowers et al., 2009](#)) leading to a variety of ages from a single rock sample. Moreover, age dispersion may also result from additional sources of  $^4\text{He}$  or the zonation of radioactive nuclides ([Vermeesch et al., 2007](#); [Ault and Flowers, 2012](#); [Gautheron et al., 2012](#)), which cannot be attributed for in thermal modelling. These issues have led to the production of an alternative analytical dating procedure utilising fragmented (or “broken”) grains, providing a wider range of thermal history constraints to improve thermal history resolution ([Beucher et al., 2013](#); [Brown et al., 2013](#)). Within this study three samples (Ka5, Ka11 and Ka15) were analysed for AHe ages, utilising both traditional whole grain and fragmented grain analysis, in an attempt to improve modelling resolution. Sample preparation and analyses is outlined in the supplementary data.

### 3.2. Thermal history modelling

Thermal history reconstructions within this study were computed using the Bayesian Transdimensional Markov Chain Monte Carlo

(MCMC) inversion within QTQt (Gallagher, 2012). AFT ages, mean track length distributions (MTL) and AHe ages are jointly inverse modelled to produce thermal histories from multiple samples across the Karrat region. This approach samples >200,000 possible thermal histories and continually assesses each one with a calculated log-likelihood function, utilising an acceptance criterion that attempts to improve predictions (Gallagher, 2012). The output is a probability distribution of model outcomes from which an 'expected model' can be produced (weighted average of the final probability distribution), yielding a thermal history derived from the resolution and quality of input data (Gallagher, 2012). This modelling approach allows for the joint inversion of multiple AFT and AHe samples from varying elevations, generating a single thermal history that correlates to all the input data and provides fundamental information regarding the thermal regime of the study area.

Grain geometry is readily accounted for within the standard thermal modelling approach, though the addition of a radiation damage model, alternative  $^4\text{He}$  diffusion parameters and resampling of the AHe error are also incorporated within this study. Radiation damage appears to significantly augment AHe ages across several passive margins (e.g., Cogné et al., 2012; Guillaume et al., 2013; Leprêtre et al., 2015; Wildman et al., 2015; Kasanzu, 2017), preserving additional  $^4\text{He}$  within vacancies in the crystal structure and increasing the calculated age. To ensure this effect is accounted for, the radiation damage model and diffusion parameters outlined in Gautheron et al. (2009) were included within thermal history modelling. This approach also permits the resampling of the additional helium activation energy required as a result of damage vacancies, believed to vary dramatically between individual grains (Gerin et al., 2017; Recanati et al., 2017), improving AHe age predictions further. Moreover, the resampling of AHe age error is also integrated within the modelling approach, increasing the error on each AHe age that repeatedly fails to conform to the rest of the input data, essentially reducing its influence on the final model output. These integrated features help produce better AHe age predictions in samples, while also effectively removing data that hinder the modelling outcome, generating thermal histories best suited to the entire dataset.

### 3.3. Landscape evolution modelling

In addition to apatite low temperature thermochronology, the application of a landscape evolution model (LEM) within this study aims to determine if the underlying geology of the region acts as a primary control on the region's topographic evolution. Modelling was carried out using FastScape (Braun and Willett, 2013), which solves the stream power law (SPL) over large areas utilising an implicit finite difference method to produce realistically eroded landscapes from an initial input geomorphology and pre-defined modelling parameters. The SPL helps compute the erosion of the landscape through time and is defined as:

$$\frac{\partial h}{\partial t} = -K_f A^m S^n$$

where  $\partial h/\partial t$  is the rate of incision,  $K_f$  is the resistance to incision,  $A$  is drainage area,  $S$  is the slope and  $m$  and  $n$  are constants. Moreover, isostatic compensation during exhumation of the landscape is calculated using a thin elastic plate model. Computed landscapes are used as interpretative tools to better understand how geomorphology has evolved through time and to isolate the key controls on its evolution.

## 4. Results

### 4.1. Apatite low temperature thermochronology

AFT central ages from the Karrat region range between  $65.77 \pm 5.1$  Ma and  $277.82 \pm 31.28$  Ma, while mean track lengths (MTLs) range between  $12.77 \pm 1.46$   $\mu\text{m}$  and  $14.43 \pm 1.53$   $\mu\text{m}$  (Table 1). Of

the 19 AFT samples 9 fail the chi-squared test ( $p < 0.05$ ), suggesting they do not form a Poisson distribution, though all but Ka11 exhibit no secondary age populations in a mixture model (Galbraith and Green, 1990). Dpar against AFT age shows a moderate positive correlation, suggesting older ages are likely sourced from slower rates of annealing in apatite, indicated by higher Dpar values (Carlson et al., 1999), while a weak correlation is observed between AFT age and uranium concentration, implying that radiation enhanced annealing may influence the final AFT ages (Hendriks and Redfield, 2005). Three samples produce anomalous ages linked to intrusive volcanism and are avoided, with Ka2 and Ka8 extracted from veins related to magmatism and Ka16 likely effected by adjacent dykes. Trends of AFT ages against elevation are consistent with an uplifted and exhumed PAZ, suggesting a significant uplift event occurred ~130 Ma (Gallagher et al., 1998). Ages above ~1000 m are consistent with the trend observed following extended residence within the PAZ, while those below 1000 m exhibit a linear trend consistent with rapid uplift (Fig. 3a) (Gallagher et al., 1998). This is further supported by the trend of MTL against elevation, which exhibits an initial increase at low elevations before decreasing following ~400 m (Fig. 3a) (Gallagher et al., 1998). Finally, AFT ages appear to decrease closer to the Nuussuaq Basin's Cretaceous boundary fault (KBF) (Fig. 3c), analogous to the AFT ages expected from an eastward escarpment retreat (Gallagher and Brown, 1999).

AHe ages from whole grains (2 T; 2 grain terminations) of the three analysed samples (Ka5; Ka11; Ka15) range between 42.0 Ma – 321.9 Ma (uncorrected) and 69.9 Ma – 473 Ma (corrected), while fragment ages (1 T; 1 grain termination) range between 10.1 Ma – 530.5 Ma (uncorrected) and 15.2 Ma – 886.1 Ma (corrected) (Table 2). For whole grain ages, trends of age against eU in Ka5 and Ka15 suggest radiation damage was evident within the grains (Flowers et al., 2009), while trends of age against the equivalent spherical grain radius ( $R'$ ) imply that grain geometry only effects Ka5. For fragment ages, trends of age against eU in only Ka15 suggest radiation damage was present, while only trends of age against fragment length in Ka11 show a correlation with grain geometry. Plots of AHe ages against compositional and geometric data can be found in the supplementary data.

Collectively these trends in the AHe data appear to demonstrate key characteristics of each sample that are crucial in understanding their age distribution and thermal histories. Ka5 appears consistent with the trends expected of slow protracted cooling through the HePRZ (Reiners and Farley, 2001; Flowers et al., 2009), Ka11 shows no obvious trends, suggesting the combination of controls has obscured any obvious trends, while the ages Ka15 appear heavily controlled by radiation damage and possibly a complex thermal history (Flowers et al., 2009; Gautheron et al., 2009). Moreover, the most obvious difference between samples is the age distributions (Fig. 3b), where Ka5 produces a tight left-skewed distribution, while Ka11 and Ka15 appear much broader and rounded, suggesting the lower elevated samples may have experienced more complex thermal histories (Fig. 3b), consistent with trends in the AFT data (Brown et al., 2013).

### 4.2. Thermal modelling

Thermal models from four separate localities across the study area have been compiled, each consisting of multiple samples: Karrat Island, Qeqertarsuaq, Ingia and Stuben (Fig. 4).

The Karrat Island dataset comprises 7 samples (7 AFT; 2 AHe) which range significantly in elevation (76 m – 734 m). Thermal modelling results exhibit accelerated cooling from 160 Ma to 110 Ma (1.7 °C/Myr), followed by a period of heating to 55 Ma (0.5 °C/Myr) and cooling to present. The latter period of cooling exhibit two phases of cooling; the first, from 55 Ma to 14 Ma, has a slow cooling rate (0.7 °C/Myr), while during the second, from 14 Ma to 0 Ma, the rate is increases (2.3 °C/Myr) (Fig. 5c). This history predicts AFT age and MTL within error, while AHe ages <120 Ma are predicted well and ages >120 Ma are predicted poorly.

**Table 1**  
Table of apatite fission track data from the Karrat Region.  $\rho_{i,s,d}$  are the respective track densities for induced, spontaneous and dosimeter tracks.  $N_{i,s,d}$  are the respective track counts for induced, spontaneous and dosimeter tracks. U is the uranium concentration of each grain ( $(\rho_i/\rho_D)[U]_{STD}$ ). Dpar is the measured length of etch pits parallel to the c-axis.  $\chi^2$  is the chi-squared value (Galbraith, 2005). Central age and age dispersion are calculated from each sample (Galbraith, 2005), and calculated from a  $\zeta$  of  $308.3 \pm 10.9$  and a dosimeter standard IRMM540. Mean track length is the average length of measured tracks that have been corrected against their c-axis values.

| Sample Number | Grains | $\rho_d (\times 10^6 \text{ cm}^{-2})$<br>(Nd) | $\rho_s (\times 10^6 \text{ cm}^{-2})$<br>(Ns) | $\rho_i (\times 10^6 \text{ cm}^{-2})$<br>(Ni) | U<br>(ppm) | Dpar<br>( $\mu\text{m}$ ) | $\chi^2$ | Age dispersion | Central Age<br>(Ma) | Mean track length<br>(corrected) ( $\mu\text{m}$ ) | Std Dev<br>( $\mu\text{m}$ ) | No of tracks | Latitude | Longitude | Elevation |
|---------------|--------|--|--|--|------------|---------------------------|----------|----------------|---------------------|--|------------------------------|--------------|----------|-----------|-----------|
| Ka1           | 20     | 1.36<br>(13002)                                | 0.27<br>(403)                                  | 0.51<br>(770)                                  | 5.66       | 1.35                      | 0.00     | 46%            | 116.55 $\pm$ 14.19  | 14.00 $\pm$ 1.12                                   | 1.21                         | 53           | 71.48    | -53.13    | 734       |
| Ka2           | 20     | 1.37<br>(13002)                                | 0.17<br>(395)                                  | 0.50<br>(1165)                                 | 5.48       | 1.29                      | 0.01     | 25%            | 67.36 $\pm$ 5.97    | 14.43 $\pm$ 1.15                                   | 1.53                         | 42           | 71.50    | -53.13    | 720       |
| Ka4           | 20     | 1.36<br>(13002)                                | 0.12<br>(194)                                  | 0.10<br>(159)                                  | 1.09       | 1.68                      | 0.99     | 0%             | 250.87 $\pm$ 26.93  | 13.47 $\pm$ 1.08                                   | 1.34                         | 33           | 71.67    | -52.00    | 1422      |
| Ka5           | 20     | 1.31<br>(13002)                                | 0.15<br>(235)                                  | 0.11<br>(171)                                  | 1.27       | 1.59                      | 0.42     | 22%            | 277.82 $\pm$ 31.28  | 13.58 $\pm$ 1.09                                   | 1.63                         | 91           | 71.69    | -52.39    | 1964      |
| Ka8           | 20     | 1.36<br>(13002)                                | 0.39<br>(393)                                  | 0.47<br>(470)                                  | 5.21       | 1.54                      | 0.39     | 3.30%          | 172.19 $\pm$ 12.16  | 12.77 $\pm$ 1.02                                   | 1.46                         | 17           | 71.52    | -52.95    | 303       |
| Ka10          | 20     | 1.34<br>(13002)                                | 0.25<br>(326)                                  | 0.45<br>(582)                                  | 5.07       | 1.47                      | 0.49     | 0%             | 114.68 $\pm$ 8.03   | 13.37 $\pm$ 1.07                                   | 1.28                         | 95           | 71.51    | -53.03    | 380       |
| Ka11          | 20     | 1.33<br>(13002)                                | 0.60<br>(835)                                  | 1.08<br>(1492)                                 | 12.15      | 1.64                      | 0.00     | 23%            | 115.86 $\pm$ 8.11   | 13.67 $\pm$ 1.09                                   | 1.31                         | 100          | 71.52    | -53.03    | 286       |
| Ka12          | 20     | 1.37<br>(13002)                                | 0.45<br>(654)                                  | 0.75<br>(1096)                                 | 8.25       | 1.25                      | 0.00     | 30%            | 117.25 $\pm$ 10.14  | 13.42 $\pm$ 1.07                                   | 1.41                         | 100          | 71.52    | -53.02    | 196       |
| Ka13          | 20     | 1.35<br>(13002)                                | 0.48<br>(467)                                  | 0.85<br>(830)                                  | 9.40       | 1.49                      | 0.30     | 12%            | 119.73 $\pm$ 8.27   | 12.88 $\pm$ 1.03                                   | 1.29                         | 65           | 71.52    | -52.99    | 160       |
| Ka14          | 20     | 1.34<br>(13002)                                | 0.29<br>(266)                                  | 0.60<br>(558)                                  | 6.77       | 1.45                      | 0.02     | 29%            | 101.85 $\pm$ 10.68  | 13.17 $\pm$ 1.05                                   | 1.38                         | 34           | 71.52    | -52.96    | 182       |
| Ka15          | 20     | 1.33<br>(13002)                                | 0.36<br>(620)                                  | 0.64<br>(1116)                                 | 7.25       | 1.59                      | 0.94     | 0%             | 112.92 $\pm$ 5.74   | 13.55 $\pm$ 1.08                                   | 1.33                         | 101          | 71.53    | -52.97    | 76        |
| Ka16          | 20     | 1.34<br>(13002)                                | 0.60<br>(270)                                  | 1.87<br>(839)                                  | 21.02      | 1.34                      | 0.30     | 13%            | 65.77 $\pm$ 5.1     | 13.77 $\pm$ 1.10                                   | 1.31                         | 71           | 71.53    | -52.88    | 78        |
| Ka21a         | 11     | 1.32<br>(13002)                                | 0.06<br>(47)                                   | 0.10<br>(80)                                   | 21.02      | 1.26                      | 0.99     | 0%             | 118.46 $\pm$ 21.8   | 14.25 $\pm$ 1.14                                   | 1.51                         | 6            | 71.63    | -52.14    | 411       |
| Ka21b         | 13     | 1.31<br>(13002)                                | 0.12<br>(103)                                  | 0.19<br>(158)                                  | 2.13       | 1.73                      | 0.60     | 21%            | 140.94 $\pm$ 20.76  | 13.69 $\pm$ 1.10                                   | 1.31                         | 10           | 71.63    | -52.14    | 411       |
| Ka22          | 20     | 1.31<br>(13002)                                | 0.26<br>(317)                                  | 0.54<br>(654)                                  | 6.23       | 1.42                      | 0.00     | 35%            | 123.72 $\pm$ 14.14  | 13.18 $\pm$ 1.05                                   | 1.28                         | 62           | 71.63    | -52.13    | 301       |
| Ka24          | 20     | 1.32<br>(13002)                                | 0.39<br>(649)                                  | 0.58<br>(968)                                  | 6.51       | 1.65                      | 0.00     | 23%            | 136.29 $\pm$ 10.19  | 13.76 $\pm$ 1.10                                   | 1.2                          | 104          | 71.62    | -52.94    | 1019      |
| Ka25          | 20     | 1.30<br>(13002)                                | 0.57<br>(1005)                                 | 0.59<br>(1043)                                 | 6.84       | 1.65                      | 0.01     | 17%            | 191.87 $\pm$ 11.76  | 13.52 $\pm$ 1.08                                   | 1.41                         | 101          | 71.62    | -52.94    | 1025      |
| Ka28          | 20     | 1.32<br>(13002)                                | 0.37<br>(579)                                  | 0.55<br>(854)                                  | 6.27       | 1.72                      | 0.07     | 17%            | 139.81 $\pm$ 9.61   | 13.87 $\pm$ 1.11                                   | 1                            | 101          | 71.87    | -53.05    | 363       |
| Ka29          | 20     | 1.35<br>(13002)                                | 0.11<br>(149)                                  | 0.34<br>(194)                                  | 3.76       | 1.13                      | 0.00     | 49%            | 93.81 $\pm$ 13.85   | 13.70 $\pm$ 1.10                                   | 1.73                         | 10           | 71.85    | -53.05    | 149       |

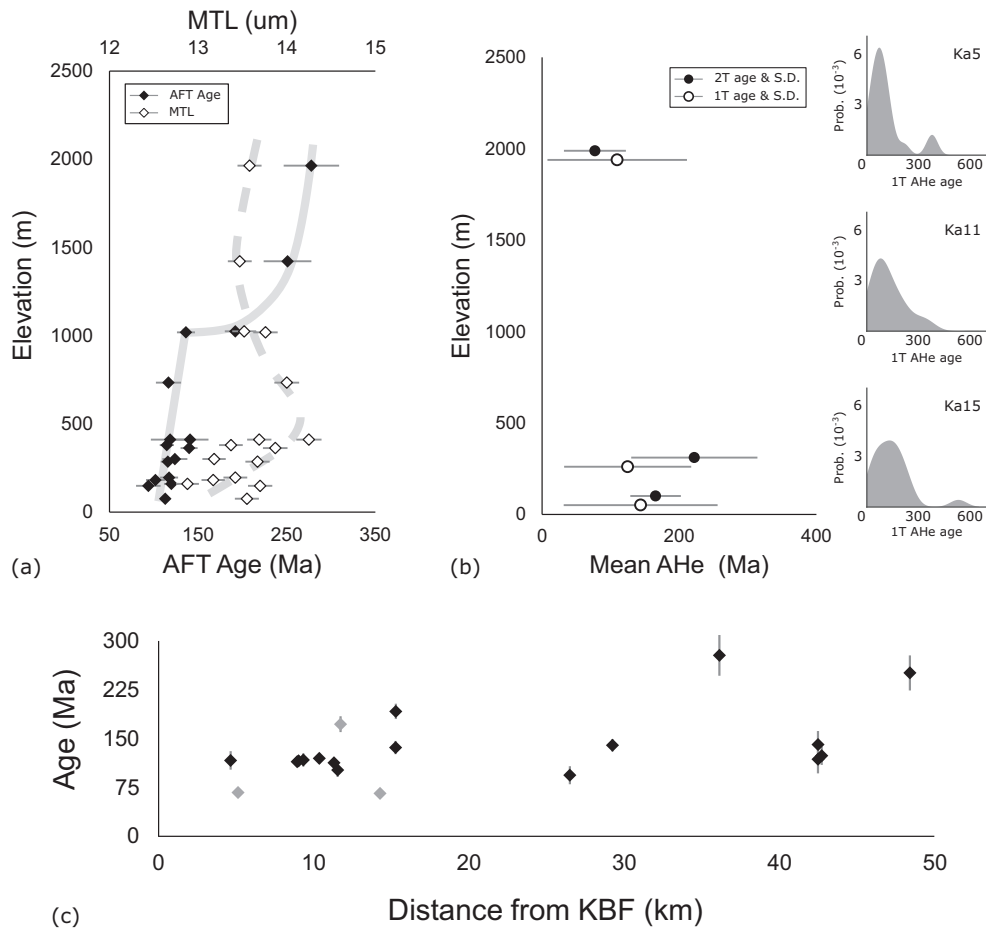


**Fig. 3.** Spatial trends of AFT and AHe data outlining key elements of the thermal history of the region. (a) AFT and MTL data against elevation: this plot outlines a trend in age that is indicative of an uplifted PAZ, where ages gradually increase initially before they increase exponentially, while MTL against elevation supports this interpretation of uplift (Gallagher et al., 1998). (b) AHe data against elevation showing weak negative trends in both 2 T and 1 T ages, though the standard deviation of all populations is large. AHe age distributions are different depending on elevation, with the distribution of the higher Ka5 appearing tight and right-skewed, while those of Ka11 and Ka15 appear much broader and rounded, implying a more complex thermal history in the lower samples (Brown et al., 2013). (c) Plot of AFT age against distance from the KBF: these exhibit generally older ages away from the KBF, implying activity along the fault may have a significant effect on the thermal histories of the region. The three discarded (volcanic) ages are coloured grey.

The Qeqertarsuaq dataset is composed of 2 AFT samples with only a minor elevation difference (1019 m – 1025 m). Thermal modelling results define linear protracted cooling from 200 Ma to 35 Ma (0.2 °C/Myr), followed by a period of accelerated cooling to present (1.2 °C/Myr) (Fig. 4a). This history predicts both age and MTL within error and is likely derived from the bell-shaped track length distributions of both samples.

The Inigia dataset is composed of 2 AFT samples from a limited elevation range (149 m - 363 m). Thermal modelling results exhibit cooling from 170 Ma to 130 Ma (1.9 °C/Myr), followed by near thermal stasis from 130 Ma to 29 Ma (0.1 °C/Myr) and a second period of cooling from 29 Ma to 0 Ma (1.9 °C/Myr) (Fig. 4b). The history predicts both age and MTL distributions within error, though Ka29 has only 10 measured track lengths, suggesting the right-skewed track distribution of Ka28 has principle control of the final history.

The Stuben dataset is composed of 4 samples (4 AFT; 1 AHe) which range significantly in elevation (301 m - 1964 m). Thermal modelling results outline near thermal stasis from 200 Ma to 142 Ma (0.1 °C/Myr), followed by an initial period of cooling from 142 Ma to 20 Ma (0.4 °C/Myr) and a second period of more accelerated cooling from 20 Ma to 0 Ma (0.8 °C/Myr) (Fig. 4d). The history predicts AFT ages and 3 of 4 MTL within error, with the MTL prediction of Ka22 overestimated by 0.3 μm, and AHe age predictions appear acceptable with only the 2 oldest ages failing to be adequately replicated.

#### 4.3. Landscape evolution modelling

The initial topography of the landscape model is defined as a sloped basaltic pile 100 km × 100 km, rising from 10 m to 1500 m (W - E) with midpoint elevation ranging from 800 m - 1000 m (Fig. 5a). The underlying geology is composed of three units, each with independent density and  $K_f$  values derived from corresponding published estimates: basalt ( $\rho = 3000 \text{ kg m}^{-3}$ ;  $K_f = 6.7 \times 10^{-6}$ ), Cretaceous sediments ( $\rho = 2200 \text{ kg m}^{-3}$ ;  $K_f = 5 \times 10^{-5}$ ) and Proterozoic basement ( $\rho = 2800 \text{ kg m}^{-3}$ ;  $K_f = 4.2 \times 10^{-6}$ ) (Fig. 6) (Stock and Montgomery, 1999; Braun et al., 2014). Additional model parameters include;  $n = 1$  and  $m = 0.3$ , to account for the tectonic setting and geology being eroded (Stock and Montgomery, 1999), while the effective elastic thickness of the lithosphere is set to 15 km (Medvedev et al., 2013). Further information regarding modelling parameters can be found in the discussion and supplementary data. Exhumation of the landscape was completed over 40 Myrs to capture the period between cessation of volcanism across West Greenland (~55 Ma) and the onset of Mid-Miocene climatic cooling (~15 Ma), where the physical weathering regime began changing dramatically (Thiede et al., 2011).

Results show exhumation of the less dense sedimentary unit becomes highly focused and localised once it is initially exposed, yet remains consistent across the basalt and basement units, generating a final landscape characterised by a low-lying trough flanked by two

**Table 2**  
Table of apatite (U–Th)/He data from the Karrat Region. eU (effective uranium) is calculated as  $[U] + 0.235[Th]$ .  $r'$  is the effective radius of each grain calculated as  $(3(\text{length}/\text{width}/2))/((2/(\text{width}/2) + \text{length}))$ . Ft is the calculated correction factor outlined in (Farley et al., 1996). Corrected age is calculated from Measured Age / Ft.

| Sample    | [He]<br>(ncc) | [U]<br>(ppm) | [Th]<br>(ppm) | [eU]<br>(ppm) | Length<br>( $\mu\text{m}$ ) | Width<br>( $\mu\text{m}$ ) | $r'$<br>( $\mu\text{m}$ ) | Ft   | Measured age<br>(Ma) |        | Corrected age<br>(Ma) |         |
|-----------|---------------|--------------|---------------|---------------|-----------------------------|----------------------------|---------------------------|------|----------------------|--------|-----------------------|---------|
| Ka5 A     | 0.054         | 1.14         | 1.94          | 1.60          | 142                         | 111                        | 59.8                      | 0.75 | 63.0                 | ± 3.2  | 84.9                  | ± 1.6   |
| Ka5 B     | 0.039         | 2.06         | 13.77         | 5.30          | 116                         | 70                         | 40.2                      | 0.63 | 42.0                 | ± 2.1  | 69.9                  | ± 5.3   |
| Ka5 C     | 0.673         | 6.67         | 1.64          | 7.05          | 147                         | 116                        | 62.5                      | 0.76 | 154.1                | ± 7.7  | 202.6                 | ± 7.0   |
| Ka5 D     | 0.041         | 3.76         | 2.97          | 4.46          | 113                         | 74                         | 41.6                      | 0.65 | 49.0                 | ± 2.4  | 77.0                  | ± 4.5   |
| Ka5-1T a  | 0.070         | 0.07         | 10.63         | 12.36         | 133                         | 154                        | 73.1                      | 0.80 | 26.3                 | ± 1.3  | 40.6                  | ± 12.4  |
| Ka5-1T b  | 0.058         | 0.06         | 2.58          | 3.11          | 83                          | 71                         | 37.2                      | 0.61 | 112.8                | ± 5.6  | 182.6                 | ± 3.1   |
| Ka5-1T d  | 0.319         | 0.32         | 235.99        | 242.51        | 97                          | 126                        | 57.3                      | 0.74 | 10.1                 | ± 0.5  | 17.1                  | ± 0.9   |
| Ka5-1T e  | 0.368         | 0.37         | 9.18          | 9.93          | 98                          | 113                        | 53.8                      | 0.72 | 368.9                | ± 18.4 | 676.3                 | ± 9.9   |
| Ka5-1T f  | 0.076         | 0.08         | 7.50          | 8.22          | 117                         | 94                         | 50.1                      | 0.70 | 124.8                | ± 6.2  | 253.5                 | ± 8.2   |
| Ka5-1T g  | 0.335         | 0.33         | 28.64         | 29.92         | 92                          | 81                         | 42.3                      | 0.65 | 217.2                | ± 10.9 | 507.4                 | ± 29.9  |
| Ka5-1T h  | 0.042         | 0.04         | 12.06         | 23.07         | 77                          | 103                        | 46.3                      | 0.68 | 49.4                 | ± 2.5  | 164.9                 | ± 23.1  |
| Ka5-1T i  | 0.043         | 0.04         | 16.57         | 22.11         | 113                         | 77                         | 42.9                      | 0.66 | 86.6                 | ± 4.3  | 457.4                 | ± 22.1  |
| Ka5-1T j  | 0.028         | 0.03         | 42.81         | 75.34         | 74                          | 68                         | 35.0                      | 0.58 | 3.5                  | ± 0.2  | 6.1                   | ± 75.3  |
| Ka5-1T k  | 0.289         | 0.29         | 35.20         | 59.11         | 96                          | 65                         | 36.5                      | 0.60 | 38.7                 | ± 1.9  | 66.1                  | ± 59.1  |
| Ka5-1T l  | 0.109         | 0.11         | 0.74          | 1.85          | 107                         | 147                        | 65.3                      | 0.77 | 81.6                 | ± 4.1  | 106.0                 | ± 1.9   |
| Ka5-1T m  | 0.451         | 0.45         | 2.86          | 5.23          | 145                         | 114                        | 61.5                      | 0.76 | 147.9                | ± 7.4  | 196.1                 | ± 5.2   |
| Ka5-1T n  | 0.043         | 0.04         | 1.39          | 2.35          | 102                         | 86                         | 45.4                      | 0.67 | 76.9                 | ± 3.8  | 115.4                 | ± 2.4   |
| Ka5-1T o  | 0.041         | 0.04         | 1.75          | 2.90          | 108                         | 86                         | 46.2                      | 0.68 | 57.6                 | ± 2.9  | 85.7                  | ± 2.9   |
| Ka5-1T p  | 0.737         | 0.74         | 0.25          | 3.48          | 108                         | 126                        | 59.8                      | 0.75 | 387.0                | ± 19.3 | 515.1                 | ± 3.5   |
| Ka5-1T q  | 0.065         | 0.07         | 1.20          | 3.05          | 71                          | 122                        | 49.4                      | 0.70 | 64.9                 | ± 3.2  | 93.2                  | ± 3.0   |
| Ka5-1T r  | 0.059         | 0.06         | 1.34          | 1.66          | 118                         | 109                        | 55.7                      | 0.73 | 81.4                 | ± 4.1  | 112.0                 | ± 1.7   |
| Ka5-1T s  | 0.048         | 0.05         | 0.66          | 1.66          | 93                          | 101                        | 48.9                      | 0.70 | 98.0                 | ± 4.9  | 141.5                 | ± 1.7   |
| Ka5-1T t  | 0.096         | 0.10         | 0.67          | 2.10          | 112                         | 107                        | 54.2                      | 0.73 | 115.8                | ± 5.8  | 160.0                 | ± 2.1   |
| Ka5-1T v  | 0.020         | 0.02         | 4.71          | 4.40          | 60                          | 78                         | 35.3                      | 0.59 | 41.4                 | ± 2.1  | 73.2                  | ± 4.4   |
| Ka11 A    | 2.395         | 26.62        | 62.41         | 41.28         | 182                         | 96                         | 56.8                      | 0.74 | 112.0                | ± 5.6  | 154.3                 | ± 41.3  |
| Ka11 C    | 1.908         | 19.51        | 10.27         | 21.92         | 118                         | 86                         | 47.2                      | 0.69 | 321.9                | ± 16.1 | 473.0                 | ± 21.9  |
| Ka11 D    | 6.952         | 38.70        | 11.62         | 41.43         | 164                         | 101                        | 58.1                      | 0.74 | 318.7                | ± 15.9 | 429.5                 | ± 41.4  |
| Ka11 G    | 0.299         | 11.31        | 6.16          | 12.76         | 106                         | 78                         | 42.6                      | 0.65 | 118.9                | ± 5.9  | 183.9                 | ± 12.8  |
| Ka11 I    | 0.674         | 7.39         | 3.19          | 8.14          | 131                         | 92                         | 51.3                      | 0.71 | 238.3                | ± 11.9 | 337.2                 | ± 8.1   |
| Ka11-1T a | 0.099         | 12.96        | 2.55          | 13.56         | 61                          | 101                        | 41.5                      | 0.65 | 38.6                 | ± 1.9  | 60.3                  | ± 13.6  |
| Ka11-1T c | 2.605         | 65.38        | 199.22        | 112.20        | 111                         | 97                         | 50.6                      | 0.71 | 73.3                 | ± 3.7  | 106.3                 | ± 112.2 |
| Ka11-1T d | 0.158         | 14.61        | 39.41         | 23.87         | 144                         | 116                        | 61.9                      | 0.76 | 11.3                 | ± 0.6  | 15.2                  | ± 23.9  |
| Ka11-1T e | 0.085         | 14.08        | 10.75         | 16.61         | 84                          | 80                         | 40.7                      | 0.64 | 31.2                 | ± 1.6  | 49.7                  | ± 16.6  |
| Ka11-1T f | 1.796         | 29.81        | 13.12         | 32.90         | 121                         | 109                        | 56.4                      | 0.74 | 123.3                | ± 6.2  | 168.2                 | ± 32.9  |
| Ka11-1T g | 0.075         | 6.78         | 2.15          | 7.28          | 95                          | 110                        | 52.3                      | 0.72 | 29.2                 | ± 1.5  | 41.0                  | ± 7.3   |
| Ka11-1T h | 5.340         | 40.26        | 20.17         | 45.00         | 121                         | 102                        | 54.0                      | 0.73 | 300.1                | ± 15.0 | 416.3                 | ± 45.0  |
| Ka11-1T i | 3.816         | 16.07        | 5.29          | 17.31         | 142                         | 118                        | 62.6                      | 0.76 | 355.3                | ± 17.8 | 467.2                 | ± 17.3  |
| Ka11-1T j | 0.117         | 18.64        | 4.16          | 19.61         | 95                          | 59                         | 33.9                      | 0.57 | 59.0                 | ± 2.9  | 105.6                 | ± 19.6  |
| Ka11-1T k | 0.914         | 17.66        | 7.29          | 19.37         | 98                          | 85                         | 44.5                      | 0.67 | 215.1                | ± 10.8 | 324.9                 | ± 19.4  |
| Ka11-1T l | 0.419         | 10.99        | 3.58          | 11.83         | 98                          | 110                        | 52.7                      | 0.72 | 98.5                 | ± 4.9  | 137.6                 | ± 11.8  |
| Ka11-1T m | 0.191         | 7.51         | 3.40          | 8.31          | 107                         | 81                         | 43.9                      | 0.66 | 107.9                | ± 5.4  | 164.2                 | ± 8.3   |
| Ka11-1T n | 0.966         | 25.61        | 11.87         | 28.40         | 84                          | 89                         | 43.5                      | 0.66 | 167.5                | ± 8.4  | 256.1                 | ± 28.4  |
| Ka11-1T o | 1.515         | 16.62        | 10.13         | 19.01         | 139                         | 105                        | 57.4                      | 0.74 | 167.3                | ± 8.4  | 227.0                 | ± 19.0  |
| Ka11-1T r | 0.218         | 19.04        | 3.31          | 19.82         | 103                         | 72                         | 40.1                      | 0.63 | 67.1                 | ± 3.4  | 106.9                 | ± 19.8  |
| Ka11-1T s | 0.542         | 15.97        | 12.35         | 18.87         | 99                          | 66                         | 37.3                      | 0.61 | 211.7                | ± 10.6 | 356.4                 | ± 18.9  |
| Ka11-1T u | 0.176         | 11.78        | 4.17          | 12.76         | 72                          | 81                         | 38.9                      | 0.62 | 95.6                 | ± 4.8  | 155.7                 | ± 12.8  |
| Ka11-1T v | 0.722         | 32.58        | 9.47          | 34.80         | 100                         | 85                         | 44.7                      | 0.67 | 94.0                 | ± 4.7  | 141.3                 | ± 34.8  |
| Ka15 A    | 1.122         | 16.49        | 4.22          | 17.48         | 159                         | 96                         | 55.1                      | 0.73 | 142.5                | ± 7.1  | 195.6                 | ± 17.5  |
| Ka15 B    | 1.105         | 16.79        | 13.93         | 20.06         | 150                         | 106                        | 58.8                      | 0.75 | 106.8                | ± 5.3  | 144.0                 | ± 20.1  |
| Ka15 C    | 1.286         | 25.58        | 23.75         | 31.16         | 106                         | 77                         | 42.2                      | 0.65 | 215.1                | ± 10.8 | 336.2                 | ± 31.2  |
| Ka15 D    | 0.967         | 18.02        | 8.52          | 20.02         | 140                         | 74                         | 43.7                      | 0.66 | 206.4                | ± 10.3 | 314.7                 | ± 20.0  |
| Ka15 E    | 0.819         | 12.92        | 10.64         | 15.42         | 133                         | 89                         | 50.0                      | 0.70 | 163.7                | ± 8.2  | 235.0                 | ± 15.4  |
| Ka15-1T a | 0.575         | 9.50         | 11.05         | 13.28         | 111                         | 89                         | 47.8                      | 0.69 | 158.6                | ± 7.9  | 232.3                 | ± 13.3  |
| Ka15-1T b | 1.739         | 28.87        | 45.65         | 52.43         | 112                         | 72                         | 40.9                      | 0.64 | 184.3                | ± 9.2  | 292.3                 | ± 52.4  |
| Ka15-1T c | 0.263         | 1.74         | 5.87          | 6.28          | 130                         | 113                        | 59.3                      | 0.75 | 81.5                 | ± 4.1  | 109.1                 | ± 6.3   |
| Ka15-1T d | 0.559         | 6.85         | 9.73          | 11.34         | 100                         | 81                         | 43.2                      | 0.66 | 243.1                | ± 12.2 | 374.2                 | ± 11.3  |
| Ka15-1T e | 0.568         | 19.18        | 17.90         | 22.40         | 73                          | 69                         | 35.0                      | 0.58 | 237.0                | ± 11.9 | 419.7                 | ± 22.4  |
| Ka15-1T f | 0.396         | 9.39         | 16.98         | 19.18         | 95                          | 80                         | 42.4                      | 0.65 | 109.5                | ± 5.5  | 169.9                 | ± 19.2  |
| Ka15-1T g | 0.768         | 52.71        | 27.91         | 40.30         | 79                          | 74                         | 37.9                      | 0.61 | 143.3                | ± 7.2  | 242.2                 | ± 40.3  |
| Ka15-1T h | 0.363         | 5.79         | 14.41         | 15.77         | 98                          | 76                         | 41.3                      | 0.64 | 130.1                | ± 6.5  | 204.5                 | ± 15.8  |
| Ka15-1T i | 0.027         | 1.88         | 5.42          | 5.87          | 89                          | 89                         | 44.4                      | 0.67 | 21.9                 | ± 1.1  | 33.0                  | ± 5.9   |
| Ka15-1T j | 0.264         | 5.61         | 10.33         | 11.65         | 105                         | 94                         | 48.6                      | 0.70 | 80.4                 | ± 4.0  | 116.5                 | ± 11.6  |
| Ka15-1T k | 1.875         | 52.03        | 58.01         | 70.23         | 64                          | 79                         | 36.7                      | 0.60 | 214.8                | ± 10.7 | 366.8                 | ± 70.2  |
| Ka15-1T l | 0.123         | 1.76         | 19.20         | 19.61         | 80                          | 96                         | 44.9                      | 0.67 | 28.2                 | ± 1.4  | 42.1                  | ± 19.6  |
| Ka15-1T m | 0.883         | 4.13         | 11.29         | 12.26         | 87                          | 70                         | 37.4                      | 0.61 | 530.5                | ± 26.5 | 886.1                 | ± 12.3  |
| Ka15-1T n | 0.497         | 2.25         | 12.21         | 12.74         | 104                         | 141                        | 63.0                      | 0.76 | 62.1                 | ± 3.1  | 81.4                  | ± 12.7  |
| Ka15-1T o | 0.035         | 1.98         | 7.27          | 7.73          | 85                          | 94                         | 45.6                      | 0.68 | 19.3                 | ± 1.0  | 28.7                  | ± 7.7   |
| Ka15-1T p | 0.150         | 2.90         | 9.66          | 10.34         | 107                         | 114                        | 55.9                      | 0.73 | 34.0                 | ± 1.7  | 46.4                  | ± 10.3  |
| Ka15-1T q | 0.620         | 19.15        | 18.98         | 23.48         | 95                          | 70                         | 38.5                      | 0.62 | 181.5                | ± 9.1  | 300.1                 | ± 23.5  |
| Ka15-1T r | 0.433         | 20.97        | 15.95         | 20.88         | 76                          | 70                         | 36.2                      | 0.60 | 177.3                | ± 8.9  | 307.6                 | ± 20.9  |
| Ka15-1T s | 0.285         | 9.60         | 17.59         | 19.84         | 77                          | 81                         | 39.7                      | 0.63 | 93.2                 | ± 4.7  | 150.2                 | ± 19.8  |
| Ka15-1T u | 0.450         | 24.00        | 26.22         | 31.86         | 67                          | 69                         | 34.2                      | 0.57 | 143.8                | ± 7.2  | 259.0                 | ± 31.9  |

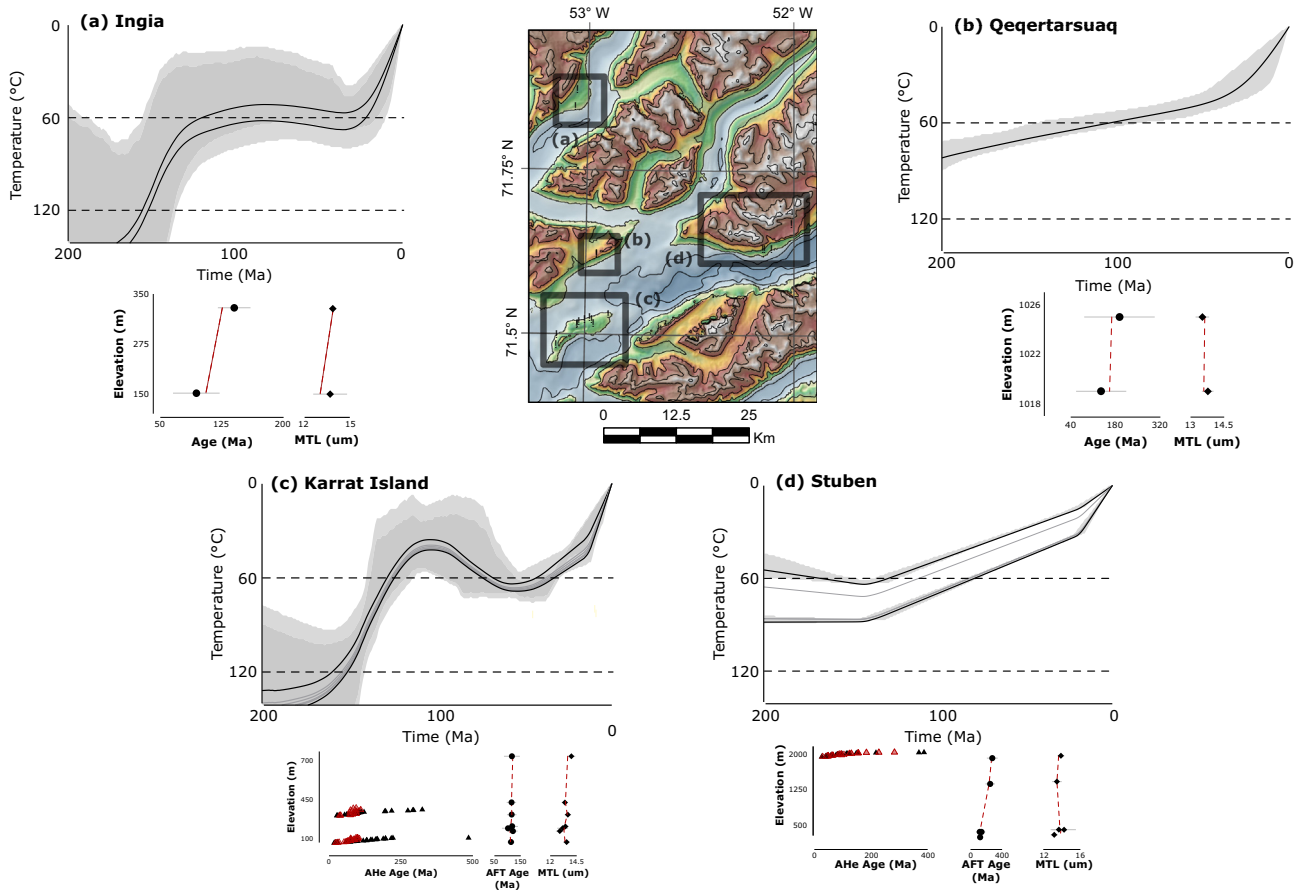


**Fig. 4.** Joint inverse thermal histories from across the Karrat region. The ‘expected’ thermal history is highlighted as a black line, while the 95% confidence for the highest and lowest samples are shown in grey. Model predictions are shown below each thermal history with the prediction for AFT and MTL shown as a dashed red line and AHe as a red triangle. (a) Qeqertarsuaq: thermal history derived from 2 AFT samples (Ka24; Ka25) exhibiting linear protracted cooling from 200 Ma to 35 Ma (0.2 °C/Myr), followed by a period of accelerated cooling to present (1.2 °C/Myr). (b) Ingia: thermal history derived from 2 Aft samples (Ka28; Ka29) displaying cooling from 170 Ma to 130 Ma (1.9 °C/Myr), followed by near thermal stasis from 130 Ma to 29 Ma (0.1 °C/Myr) and a second period of cooling from 29 Ma to 0 Ma (1.9 °C/Myr). (c) Karrat Island: thermal history derived from 7 AFT and 2 AHe samples (Ka1; Ka10; Ka11; Ka12; Ka13; Ka14; Ka15) showing accelerated cooling from 160 Ma to 110 Ma (1.7 °C/Myr), followed by a period of heating to 55 Ma (0.5 °C/Myr) and cooling to 0 Ma. (d) Stuben: thermal history derived from 4 AFT and 1 AHe sample(s) (Ka4; Ka5; Ka21; Ka22) exhibiting outline near thermal stasis from 200 Ma to 142 Ma (0.1 °C/Myr), followed by cooling from 142 Ma to 0 Ma (0.45 °C/Myr). Each thermal history provides AFT and MTL prediction with in error, with the exception of Ka22 MTL, which is over predicted by 0.3 μm, while AHe ages >120 Ma in samples Ka11 and Ka15 fail to provide adequate predictions.

escarpments to the east and west (Fig. 5). Cumulative rock uplift in response to exhumation during the 40 Myrs of model time ranges between 322.4 m – 167.8 m, with the highest values at the base of the basement escarpment and lowest at the model peripheries (Fig. 5c). Additionally, the sedimentary yield through time exhibits three key periods: an initial rapidly increasing output (0 Myrs – 5 Myrs; 55 Ma – 50 Ma), a more gradual rise in output following initial exposure of the underlying units (5 Myrs – 18 Myrs; 50 Ma – 37 Ma) and a decline of sediment output following the onset of localised exhumation (18 Myrs – 40 Myrs; 37 Ma – 15 Ma) (Fig. 5b).

## 5. Discussion

### 5.1. Topographic evolution of the Karrat region

The AFT/AHe results, thermal histories and LEM presented here imply much of the topography in the Karrat region is derived from rift flank uplift along the KBF and has since been preserved by widespread volcanism, differential erosion and isostatic uplift.

Uplift of the region likely began during rifting in the Early-Cretaceous and the opening of the Nuussuaq Basin. The trends of AFT ages and MTL against elevation in the region are indicative of significant uplift across Karrat ~130 Ma (Fig. 2), most likely along the footwall of the KBF (Fig. 6a). This is corroborated by thermal histories adjacent

to the KBF that exhibit accelerated cooling between 170 Ma and 110 Ma (Fig. 4a/c), while inland thermal histories exhibit only protracted cooling (Fig. 4d), likely representing the increase in exhumation rate along the fault during uplift and lower rates further inland. Moreover, stratigraphy observed on Upernivik Ø and Qeqertarsuaq records the existence of a laterally migrating syn-tectonic braided fluvial systems in the Mid-Cretaceous adjacent to the KBF, likely a response to tectonism and uplift across the fault (Koch, 1964; Dam et al., 2009).

Tectonic quiescence appears to follow this early phase of uplift, allowing for the accumulation of fluvial sediments and volcanics during the development of the Nuussuaq Basin and its eventual fill. Thermal histories derived from locations closest to the KBF each display either thermal stasis or reheating between 110 Ma and 55 Ma or 25 Ma (Fig. 4), suggesting the rate of uplift decreased, allowing sediment to accumulate (Fig. 6b). This is corroborated by the later stratigraphy from Upernivik Ø and Qeqertarsuaq, outlining a period of low energy estuarine/coastal environments in the Late Cretaceous characterised by finer grain sizes and bioturbation (Dam et al., 2009). Furthermore, the presence of volcanic strata atop the margin and the lack of heating in the Stuben thermal model suggests the basement escarpment likely remained at height during volcanism and experienced only limited burial (Fig. 6c).

The period following the end of volcanism is dominated by widespread cooling in each thermal history model, with the rate of cooling

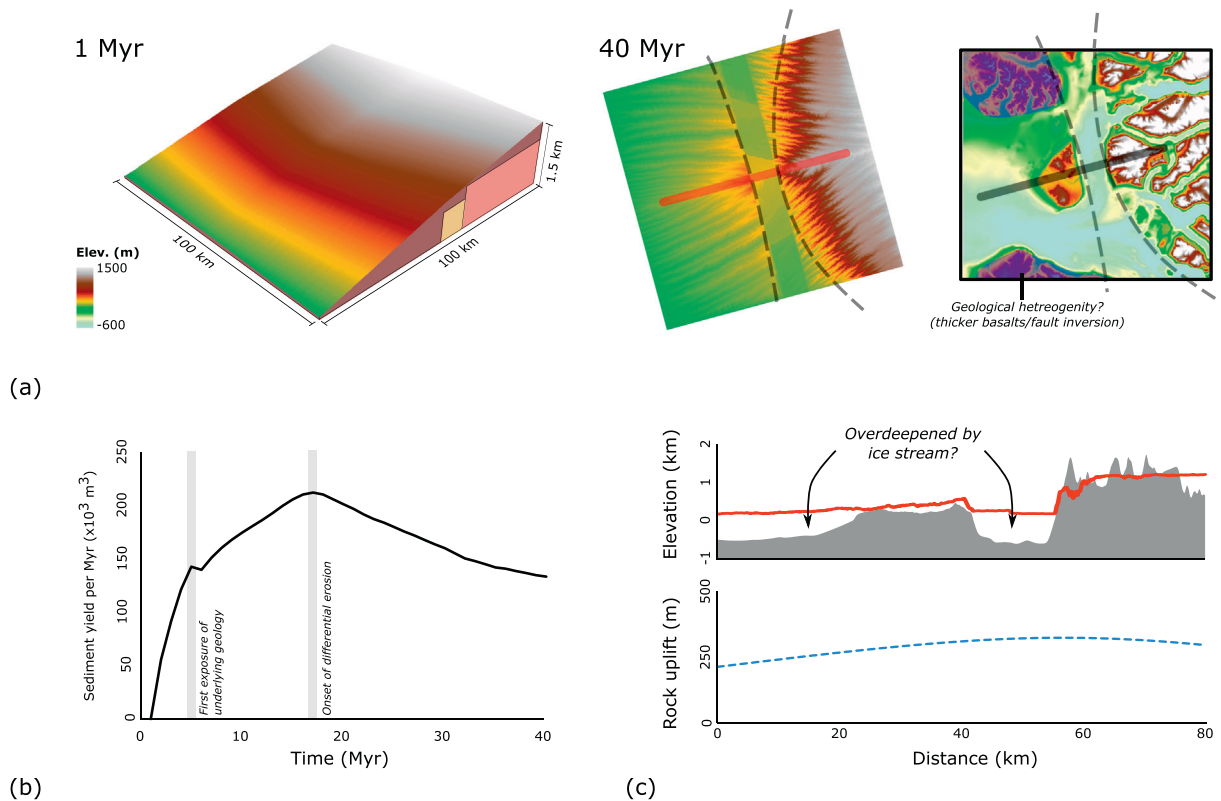


**Fig. 5.** Result of FastScape landscape evolution model run to test differential exhumation of the region. (a) Initial model conditions are shown in the top left, with a sloped volcanic pile underlain by two units, one a weaker “sedimentary” unit and the second being “basement”. Crucially, the z-axis is not to scale and has been exaggerated to ensure the underlying lithologies are visible. Results of the model are shown in the top right, showing that after 40 Myrs of exhumation a landscape displaying similar characteristics to the modern geomorphology. (b) The sedimentary yield per million year during the modelled 40 Myrs shows three distinct periods separated by the initial exposure of the underlying basement units and the onset of localised differential erosion. (c) Cross sections of both the model and modern landscapes highlight the similarities between the two, with both elevated regions being separated by a region of low-lying topography. It is conceivable that following the onset of glaciation the lower lying areas would experience deep glacial scouring, decreasing the elevation further, while higher topography areas could see an increase in elevation, similar to the pre-glacial landscape produced in [Gołędowski et al. \(2013\)](#). Further information regarding FastScape modelling can be found in the supplementary data.

increasing at various points in the late Cenozoic. This cooling may be argued to result from exhumation of the landscape following episodic uplift during the late Cenozoic, as implied by the interpretations of peneplains in the landscape ([Japsen et al., 2006](#)). However, such an interpretation has been contentiously debated within the literature, with a plausible source for tectonic uplift yet to be outlined and other alternative non-tectonic explanations available (e.g., [Egholm et al., 2017](#); [Strunk et al., 2017](#)). Instead, cooling more likely represents the prolonged exhumation of the volcanic pile, following the end of lava extrusion. This widespread exhumation of the volcanic pile is depicted in the results of the LEM, illustrating intense localised erosion of the underlying geological units was likely dominant in the region following volcanism and has shaped the complex pre-glacial geomorphology. Moreover, exhumation appears to drive up to ~300 m of isostatic response from the lithosphere uplifting the basement and volcanic escarpments and further exaggerating the region’s undulating geomorphology. This interpretation of the post-volcanic history negates the need for uplift across the region and suggests how the elevated topography was likely present at the onset of glaciation.

The onset of glaciation in the region was undoubtedly vital in creating the modern geomorphology, influencing the near surface thermal regime and protecting much of the highest topography from intense erosion. The thermal history of Karrat Island ([Fig. 4c](#)) exhibits a second phase of more intense cooling from the Miocene onwards, synchronous to the onset of climate deterioration and glaciation across Greenland ([Eldrett et al., 2009](#); [Thiede et al., 2011](#)), implying more intense glacial erosion affected the thermal regime ([Fig. 6d](#)). Additionally, cosmogenic radionuclide ages from across the basement demonstrate selective linear erosion of the basement rock was highly effective during glaciation

and likely led to widespread exhumation of the region, creating much of the modern fjordal geomorphology ([Roberts et al., 2013](#); [Lane et al., 2014](#)). On Quaternary timescales ([Schaefer et al., 2016](#); [Strunk et al., 2017](#)), this process can lead to the effective preservation of higher topography, as lower exhumation rates persist at greater elevations ([Egholm et al., 2017](#)), and the deepening of fjords and troughs, removing vast quantities of rock and producing a positive isostatic response from the lithosphere. The effect of this processes on the pre-glacial landscape implied by the LEM would likely encourage the coalescence of outlet glaciers within the low-lying trough, instigating the early development of the Uummannaq Ice Stream. This combination of selective linear erosion, over-deepening, topographic preservation and isostatic uplift are likely all fundamental in maintaining the hypsometry of the modern landscape.

### 5.2. Wider implications for glaciated margins

The wider geomorphology of the Nuussuaq Basin remains a controversial topic, as some authors interpret the elevated topography to have been produced from late Cenozoic tectonic uplift ([Bonow et al., 2006](#); [Japsen et al., 2006](#)), while others suggest it is the result of widespread exhumation, generating  $\leq 800$  m of isostatic uplift since the Neogene ([Medvedev et al., 2013](#)). The principal evidence for episodic uplift across the region is the interpretation of peneplains (uplifted floodplains) in the landscape and marine fossils observed at ~1100 m on the Nuussuaq Peninsula, though neither are diagnostic indicators of post-rift tectonism. The interpretation of peneplains remains highly controversial, with many authors questioning their validity as indicators of uplift (e.g., [Bishop, 2007](#); [Gregory and Goudie, 2011](#)) and others suggesting

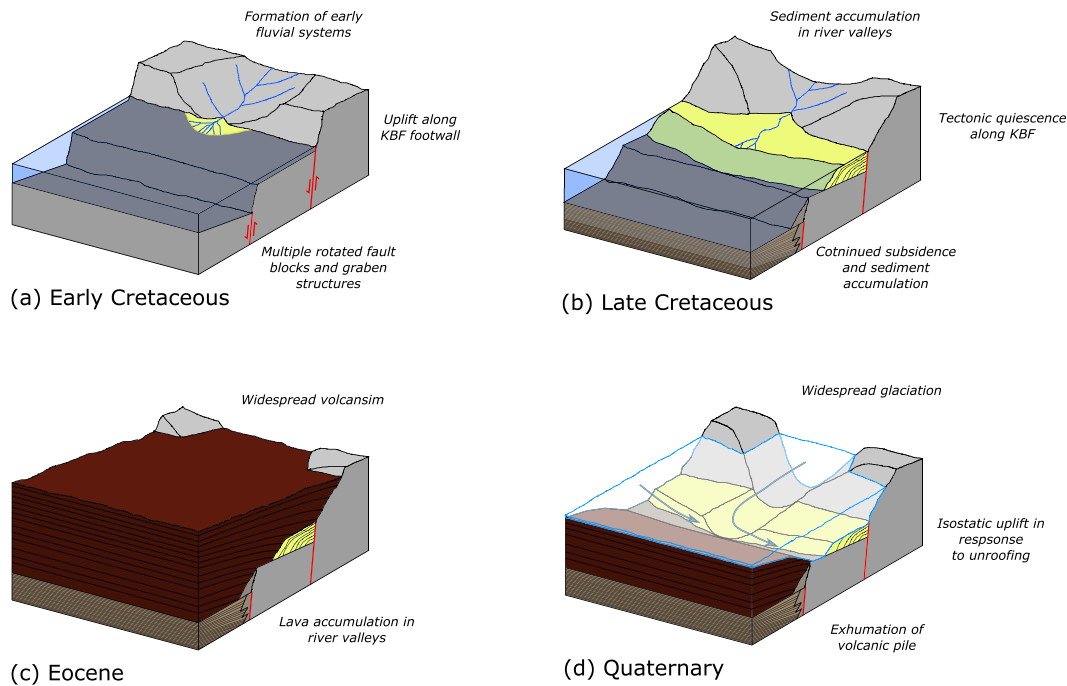


**Fig. 6.** Cartoon outlining the topographic evolution of the Karrat region. (a) Early Cretaceous: significant tectonic uplift occurs along the footwall of the KBF instigated the erosion of the footwall by early syn-tectonic fluvial systems. (b) Late Cretaceous: tectonic quiescence following uplift allows major fluvial systems to prograde out into the basin bury portions of the margin in sediment. (c) Eocene: widespread volcanism spreads east and west, burying much of the Cretaceous river valleys in lava, protecting the rift flank for further exhumation. (d) Quaternary: widespread exhumation following the end of volcanism removes much of the volcanic pile, while selective linear erosion removes large quantities of rock and preserve the highest topography.

they result from differential glacial erosion and not tectonic uplift (Egholm et al., 2017; Strunk et al., 2017). Moreover, while the elevation of the marine fossils defines the extent of uplift following the Early Palaeocene, it fails to provide insight into the processes driving uplift, suggesting both isostasy and thermally-induced doming associated with volcanism may be considered viable uplift mechanisms (Medvedev et al., 2013; Jess et al., 2018).

The results and interpretations of this study are more supportive of exhumation and isostatic uplift rather than tectonic uplift, given that the thermal models predict widespread cooling from the Eocene to present, consistent with histories from the Nuussuaq Basin itself (Jess et al., 2018). Additionally, results of the LEM demonstrate how differential exhumation may have prompted ~300 m of isostatic uplift prior to ~15 Ma, suggesting exhumation of the landscape likely produce significant rock uplift, consistent with the conclusions of Medvedev et al. (2013). This interpretation of the region's evolution promotes continuous exhumation as the leading factor of uplift across the margin during its post-rift stage and does not seek further tectonism to drive uplift across the region. Secondary sources of uplift across the region may relate to volcanism, with the emplacement of thick igneous intrusions and thermal-doming of the lithosphere both likely to cause further uplift of the landscape during the Palaeocene.

In addition to estimates of uplift, the results of the LEM also have wider implications regarding the geomorphology of glaciated Atlantic margins and their underlying geology. Elevated topography across East Greenland, Norway and Scotland all exhibit considerable marked glacial geomorphology with over-deepened troughs and preserved high elevation plateaux. In each case, there is likely a link with underlying geology and pre-glacial landscape: many of the characteristics of fjords across East Greenland have been previously attributed to the changes in underlying rock lithology (Swift et al., 2008), while analysis of the Scottish Highlands determined underlying rock strength has a first order control on glacial geometries (Brook et al., 2004). Moreover, the complex fjordal morphology of the UIS may also derive from the pre-glacial drainage system that differential eroded the volcanic pile

and has been highly influenced by the paleo-topography; a characteristic noted across other major glacial system on Greenland (Bamber et al., 2013; Cooper et al., 2016). These observations collectively suggest much of the glacially driven geomorphological development across Greenland and other passive continental margins may result from a combination of underlying geology, pre-glacial landscape evolution and ice sheet dynamics.

### 5.3. Dispersion in AHe data: an indicator of Palaeozoic burial?

The addition of AHe ages in two of the thermal models does assist in resolving thermal histories and reducing confidence intervals, compared to thermal histories without AHe data. However, AHe ages >120 Ma within the Karrat thermal history are not effectively modelled, implying additional  $^4\text{He}$  was present within grains and suggesting the presence of either unobservable  $^4\text{He}$  sources (e.g., implantation, micro-inclusions, zonation) or a more complex pre-rift history. The destructive nature of AHe analysis makes it hard to characterise each grain individually, suggesting a catalogue of issues may be responsible, such as implantation, micro-inclusions or zonation of parent nuclides. These issues are considered to be fundamental causes of age dispersion in AHe samples (Ketcham et al., 2011; Gautheron et al., 2012; Zeitler et al., 2017), though a complex pre-rift history resulting from the accumulation of sediment across Laurentia in the Palaeozoic may also be considered (Flowers et al., 2012; Ault et al., 2013). Burial of samples past ~120 °C is believed to anneal radiation damage vacancies within apatite (Flowers et al., 2009; Gautheron et al., 2009), though some authors postulate vacancies may remain, leading to additional  $^4\text{He}$  remaining within apatites and increasing the final age (Fox and Shuster, 2014). This under-annealing of damage vacancies combined with a pre-rift burial history could increase the ages of higher eU apatites and produce the wider spread of ages seen in AHe samples. Both interpretations of the older AHe ages may help explain the wide dispersion of AHe age in passive margin datasets and encourages

further work on the subject, though it is difficult to test their viability with current levels of knowledge.

#### 5.4. Landscape evolution model: uncertainties

Limitations and uncertainties are inherent within the LEM. The initial assumption of steady-state topography is in place to simplify the results and reduce processing time and, as such, this model should not be considered as providing a realistic simulation of regional exhumation, but simply to highlight the importance of rock strength in the exhumational process. Additionally, the three fundamental uncertainties are the scaling factors of the stream power law ( $n$ ,  $m$ ,  $K_f$ ), effective elastic thickness of the lithosphere (EET) and the post-volcanic elevation. Scaling factors  $n$  and  $m$  vary depending on tectonic setting, climate and lithology and can greatly affect model outputs, therefore values were specifically selected to best suit the passive margin setting, the geology being eroded and simplify the modelling process (Stock and Montgomery, 1999). Altering of the  $K_f$  value for the central sedimentary unit only changes the rate at which the unit erodes (supplementary data) and the initial value should be regarded as conservative, considering the considerable content of weaker mudstone within the Cretaceous sediments (Stock and Montgomery, 1999; Dam et al., 2009). Changing of the EET value across the model affects the total maximum isostatic uplift computed (25 km = 101 m; 5 km = 1305 m), though the value used in Medvedev et al. (2013) does appear best suited to rifted cratonic lithosphere of the study area. Finally, the maximum post volcanic height of 1500 m is estimated from outcrops of lavas atop the basement margins found at this height, though raising or lowering this maximum elevation appears to only control the final height of the basement escarpment (supplementary data). These uncertainties are apparent within the LEM, though the broad and simplistic nature of the model is suitable for the aim of the study and helps to establish how differential erosion of the underlying geological units shapes the landscape.

## 6. Summary and conclusions

Low temperature thermochronology and landscape evolution modelling from across the Karrat region of central West Greenland reveals a history dominated by rifting in the Mesozoic and widespread erosion in the Cenozoic. The combination of AFT and AHe data, joint inverse thermal history modelling and landscape evolution modelling demonstrates how the modern topography formed from rift flank uplift in the Cretaceous that has since been preserved by volcanic cover and differential erosion.

The topography across the basin margin likely formed during rifting in the Cretaceous, generated from considerable uplift of the KBF footwall. Sedimentary deposition and volcanism in the Palaeogene followed, burying low lying areas of the region, while also protecting the elevated rift flank from further erosion throughout the Early Cenozoic. Widespread erosion is interpreted following the end of volcanism and is believed to remove much of the volcanic pile and induce a significant isostatic response from the lithosphere (~300 m), uplifting the topography further. Moreover, differential exhumation of the underlying geology in the late Cenozoic may also be the source of the postulated pre-glacial landscape that acted as the precursor for the development and unique geometry of the Uummannaq Ice Stream onset zone that dominates the modern geomorphology of the region. This interpretation of the regional landscape evolution suggests that the modern topography is the result of rift flank uplift in the Cretaceous and preserved by volcanism and differential erosion thereafter, negating any requirement for late Cenozoic episodic, tectonic uplift.

## Acknowledgements

Brice Rea and Tim Lane are sincerely thanked for the collection of samples, while Robert McDonald, Andy Carter and James Schwanethal

are also thanked for their assistance in sample preparation and analysis. The work contained in this publication contains work conducted during a PhD study undertaken as part of the Natural Environment Research Council (NERC) Centre for Doctoral Training (CDT) in Oil and Gas [grant number NEM00578X/1] and is sponsored by the University of Aberdeen.

## Appendix A. Supplementary data

Supplementary data to this article can be found online at <https://doi.org/10.1016/j.geomorph.2019.02.026>.

## References

- Anell, I., Thybo, H., Artemieva, I.M., 2009. Cenozoic uplift and subsidence in the North Atlantic region: geological evidence revisited. *Tectonophysics* 474 (1–2), 78–105.
- Ault, A.K., Flowers, R.M., 2012. Is apatite U–Th zonation information necessary for accurate interpretation of apatite (U–Th)/He thermochronometry data? *Geochim. Cosmochim. Acta* 79, 60–78.
- Ault, A.K., Flowers, R.M., Bowring, S.A., 2013. Phanerozoic surface history of the Slave craton. *Tectonics* 32 (5), 1066–1083.
- Bamber, J.L., Siegert, M.J., Griggs, J.A., Marshall, S.J., Spada, G., 2013. Paleofluvial megacanyon beneath the central Greenland ice sheet. *Science* 341 (6149), 997–999.
- Beucher, R., Brown, R.W., Roper, S., Stuart, F., Persano, C., 2013. Natural age dispersion arising from the analysis of broken crystals: part II. Practical application to apatite (U–Th)/He thermochronometry. *Geochim. Cosmochim. Acta* 120, 395–416.
- Bishop, P., 2007. Long-term landscape evolution: linking tectonics and surface processes. *Earth Surf. Process. Landf.* 32 (3), 329–365.
- Bonow, J.M., Japsen, P., Lidmar-Bergström, K., Chalmers, J.A., Pedersen, A.K., 2006. Cenozoic uplift of Nuussuaq and Disko, West Greenland—elevated erosion surfaces as uplift markers of a passive margin. *Geomorphology* 80 (3–4), 325–337.
- Bonow, J.M., Japsen, P., Nielsen, T.F., 2014. High-level landscapes along the margin of southern East Greenland—a record of tectonic uplift and incision after breakup in the NE Atlantic. *Glob. Planet. Chang.* 116, 10–29.
- Braun, J., Willett, S.D., 2013. A very efficient O (n), implicit and parallel method to solve the stream power equation governing fluvial incision and landscape evolution. *Geomorphology* 180, 170–179.
- Braun, J., Simon-Labric, T., Murray, K.E., Reiners, P.W., 2014. Topographic relief driven by variations in surface rock density. *Nat. Geosci.* 7 (7), 534.
- Brook, M.S., Kirkbride, M.P., Brock, B.W., 2004. Rock strength and development of glacial valley morphology in the Scottish Highlands and northwest Iceland. *Geografiska Annaler: Series A, Phys. Geogr.* 86 (3), 225–234.
- Brown, R.W., Beucher, R., Roper, S., Persano, C., Stuart, F., Fitzgerald, P., 2013. Natural age dispersion arising from the analysis of broken crystals. Part I: theoretical basis and implications for the apatite (U–Th)/He thermochronometer. *Geochim. Cosmochim. Acta* 122, 478–497.
- Carlson, W.D., Donelick, R.A., Ketcham, R.A., 1999. Variability of apatite fission-track annealing kinetics: I. Experimental results. *Am. Mineral.* 84 (9), 1213–1223.
- Chalmers, J.A., 2000. Offshore evidence for Neogene uplift in central West Greenland. *Glob. Planet. Chang.* 24 (3–4), 311–318.
- Cogné, N., Gallagher, K., Cobbold, P.R., Riccomini, C., Gautheron, C., 2012. Post-breakup tectonics in southeast Brazil from thermochronological data and combined inverse-forward thermal history modeling. *J. Geophys. Res. Solid Earth* 117 (B11).
- Cooper, M.A., Michaelides, K., Siegert, M.J., Bamber, J.L., 2016. Paleofluvial landscape inheritance for Jakobshavn Isbræ catchment, Greenland. *Geophys. Res. Lett.* 43 (12), 6350–6357.
- Dam, G., Nøhr-Hansen, H., Christiansen, F.G., Bojesen-Koefoed, J.A., Laiert, T., 1998a. The oldest marine Cretaceous sediments in West Greenland (Umiivik-1 borehole): record of the Cenomanian-Turonian anoxic event? *Geol. Greenl. Surv. Bull.* 180, 128–137.
- Dam, G., Larsen, M., Sønderholm, M., 1998b. Sedimentary response to mantle plumes: Implications from Paleocene onshore successions, West and East Greenland. *Geology* 26 (3), 207–210.
- Dam, G., Pedersen, G.K., Sønderholm, M., Midtgård, H., Larsen, L.M., Nøhr-Hansen, H., Pedersen, A.K., 2009. Lithostratigraphy of the Cretaceous–Paleocene Nuussuaq Group, Nuussuaq Basin, West Greenland. *Geological Survey of Denmark and Greenland Bulletin* 19, 01–171.
- Dumitru, T.A., 1993. A new computer-automated microscope stage system for fission-track analysis. *Nucl. Tracks Radiat. Meas.* 21 (4), 575–580.
- Egholm, D.L., Jansen, J.D., Brædstrup, C.F., Pedersen, V.K., Andersen, J.L., Ugelvig, S.V., Larsen, N.K., Knudsen, M.F., 2017. Formation of plateau landscapes on glaciated continental margins. *Nat. Geosci.* 10 (8), 592.
- Eidvin, T., Riis, F., Rasmussen, E.S., 2014. Oligocene to Lower Pliocene deposits of the Norwegian continental shelf, Norwegian Sea, Svalbard, Denmark and their relation to the uplift of Fennoscandia: a synthesis. *Mar. Pet. Geol.* 56, 184–221.
- Eldrett, J.S., Greenwood, D.R., Harding, I.C., Huber, M., 2009. Increased seasonality through the Eocene to Oligocene transition in northern high latitudes. *Nature* 459 (7249), 969.
- Farley, K.A., 2000. Helium diffusion from apatite: General behavior as illustrated by Durango fluorapatite. *J. Geophys. Res. Solid Earth* 105 (B2), 2903–2914.
- Farley, K.A., Wolf, R.A., Silver, L.T., 1996. The effects of long alpha-stopping distances on (U–Th)/He ages. *Geochim. Cosmochim. Acta* 60 (21), 4223–4229.

- Flowers, R.M., Ketcham, R.A., Shuster, D.L., Farley, K.A., 2009. Apatite (U–Th)/He thermochronometry using a radiation damage accumulation and annealing model. *Geochim. Cosmochim. Acta* 73 (8), 2347–2365.
- Flowers, R.M., Ault, A.K., Kelley, S.A., Zhang, N., Zhong, S., 2012. Epeirogeny or eustasy? Paleozoic–Mesozoic vertical motion of the North American continental interior from thermochronometry and implications for mantle dynamics. *Earth Planet. Sci. Lett.* 317, 436–445.
- Fox, M., Shuster, D.L., 2014. The influence of burial heating on the (U–Th)/He system in apatite: Grand Canyon case study. *Earth Planet. Sci. Lett.* 397, 174–183.
- Galbraith, R.F., 2005. Statistics for Fission Track Analysis. Chapman and Hall/CRC.
- Galbraith, R.F., Green, P.F., 1990. Estimating the component ages in a finite mixture. *International Journal of Radiation Applications and Instrumentation. Part D. Nucl. Tracks Radiat. Meas.* 17 (3), 197–206.
- Gallagher, K., 2012. Transdimensional inverse thermal history modeling for quantitative thermochronology. *J. Geophys. Res. Solid Earth* 117 (B2).
- Gallagher, K., Brown, R., 1999. Denudation and uplift at passive margins: the record on the Atlantic Margin of southern Africa. *Philosophical Transactions of the Royal Society of London. Series A: Math. Phys. Eng. Sci* 357 (1753), 835–859.
- Gallagher, K., Brown, R., Johnson, C., 1998. Fission track analysis and its applications to geological problems. *Annu. Rev. Earth Planet. Sci.* 26 (1), 519–572.
- Gautheron, C., Tassan-Got, L., Barbarand, J., Pagel, M., 2009. Effect of alpha-damage annealing on apatite (U–Th)/He thermochronology. *Chem. Geol.* 266 (3–4), 157–170.
- Gautheron, C., Tassan-Got, L., Ketcham, R.A., Dobson, K.J., 2012. Accounting for long alpha-particle stopping distances in (U–Th–Sm)/He geochronology: 3D modeling of diffusion, zoning, implantation, and abrasion. *Geochim. Cosmochim. Acta* 96, 44–56.
- Gerin, C., Gautheron, C., Oliviero, E., Bachelet, C., Djimbi, D.M., Seydoux-Guillaume, A.M., Tassan-Got, L., Sarda, P., Roques, J., Garrido, F., 2017. Influence of vacancy damage on He diffusion in apatite, investigated at atomic to mineralogical scales. *Geochim. Cosmochim. Acta* 197, 87–103.
- Gołędowski, B., Egholm, D.L., Nielsen, S.B., Clausen, O.R., McGregor, E.D., 2013. Cenozoic erosion and flexural isostasy of Scandinavia. *J. Geodyn.* 70, 49–57.
- Green, P.F., 1989. Thermal and tectonic history of the East Midlands shelf (onshore UK) and surrounding regions assessed by apatite fission track analysis. *J. Geol. Soc.* 146 (5), 755–773.
- Green, P.F., Japsen, P., Chalmers, J.A., Bonow, J.M., Duddy, I.R., 2018. Post-breakup burial and exhumation of passive continental margins: seven propositions to inform geodynamic models. *Gondwana Res.* 53, 58–81.
- Gregory, K.J., Goudie, A.S. (Eds.), 2011. *The SAGE Handbook of Geomorphology*. Sage Publications.
- Grocott, J., McCaffrey, K.J., 2017. Basin evolution and destruction in an Early Proterozoic continental margin: the Rinkian fold–thrust belt of central West Greenland. *J. Geol. Soc.* 174 (3), 453–467.
- Guillaume, B., Gautheron, C., Simon-Labric, T., Martinod, J., Roddaz, M., Douville, E., 2013. Dynamic topography control on Patagonian relief evolution as inferred from low temperature thermochronology. *Earth Planet. Sci. Lett.* 364, 157–167.
- Hansen, S., 1996. Quantification of net uplift and erosion on the Norwegian Shelf south of 66°N from sonic transit times of shale. *Nor. Geol. Tidsskr.* 76, 245–252.
- Hendriks, B.W., Andriessen, P.A., 2002. Pattern and timing of the post-Caledonian denudation of northern Scandinavia constrained by apatite fission-track thermochronology. *Geol. Soc. Lond. Spec. Publ.* 196 (1), 117–137.
- Hendriks, B.W.H., Redfield, T.F., 2005. Apatite fission track and (U–Th)/He data from Fennoscandia: an example of underestimation of fission track annealing in apatite. *Earth Planet. Sci. Lett.* 236 (1–2), 443–458.
- Japsen, P., 1998. Regional velocity–depth anomalies, North Sea Chalk: a record of overpressure and Neogene uplift and erosion. *AAPG Bull.* 82 (11), 2031–2074.
- Japsen, P., Chalmers, J.A., 2000. Neogene uplift and tectonics around the North Atlantic: overview. *Glob. Planet. Chang.* 24 (3–4), 165–173.
- Japsen, P., Green, P.F., Chalmers, J.A., 2005. Separation of Palaeogene and Neogene uplift on Nuussuaq, West Greenland. *J. Geol. Soc.* 162 (2), 299–314.
- Japsen, P., Bonow, J.M., Green, P.F., Chalmers, J.A., Lidmar-Bergström, K., 2006. Elevated, passive continental margins: long-term highs or Neogene uplifts? New evidence from West Greenland. *Earth Planet. Sci. Lett.* 248 (1–2), 330–339.
- Japsen, P., Green, P.F., Bonow, J.M., Nielsen, T.F., Chalmers, J.A., 2014. From volcanic plains to glaciated peaks: burial, uplift and exhumation history of southern East Greenland after opening of the NE Atlantic. *Glob. Planet. Chang.* 116, 91–114.
- Jess, S., Stephenson, R., Brown, R., 2018. Evolution of the central West Greenland margin and the Nuussuaq Basin: localised basin uplift along a stable continental margin proposed from thermochronological data. *Basin Res.* 30 (6), 1230–1246.
- Kasanzu, C.H., 2017. Apatite fission track and (U–Th)/He thermochronology from the Archean Tanzania Craton: contributions to cooling histories of Tanzanian basement rocks. *Geosci. Front.* 8 (5), 999–1007.
- Ketcham, R.A., Gautheron, C., Tassan-Got, L., 2011. Accounting for long alpha-particle stopping distances in (U–Th–Sm)/He geochronology: Refinement of the baseline cas. *Geochim. Cosmochim. Acta* 75 (24), 7779–7791.
- Koch, B.E., 1964. Review of fossil flora and nonmarine deposits of West Greenland. *Geol. Soc. Am. Bull.* 75 (6), 535–548.
- Lane, T.P., Roberts, D.H., Rea, B.R., Cofaigh, C.Ó., Viel, A., Rodés, A., 2014. Controls upon the Last Glacial maximum deglaciation of the northern Uummannaq ice stream system, West Greenland. *Quat. Sci. Rev.* 92, 324–344.
- Larsen, L.M., Heaman, L.M., Creaser, R.A., Duncan, R.A., Frei, R., Hutchison, M., 2009. Tectonomagmatic events during stretching and basin formation in the Labrador Sea and the Davis Strait: evidence from age and composition of Mesozoic to Palaeogene dyke swarms in West Greenland. *J. Geol. Soc.* 166 (6), 999–1012.
- Larsen, L.M., Pedersen, A.K., Tegner, C., Duncan, R.A., Hald, N., Larsen, J.G., 2016. Age of Tertiary volcanic rocks on the West Greenland continental margin: volcanic evolution and event correlation to other parts of the North Atlantic Igneous Province. *Geol. Mag.* 153 (3), 487–511.
- Leprêtre, R., Misseand, Y., Barbarand, J., Gautheron, C., Saddiqi, O., Pinna-Jamme, R., 2015. Postrift history of the eastern central Atlantic passive margin: insights from the Saharan region of South Morocco. *J. Geophys. Res. Solid Earth* 120 (6), 4645–4666.
- Medvedev, S., Hartz, E.H., 2015. Evolution of topography of post-Devonian Scandinavia: effects and rates of erosion. *Geomorphology* 231, 229–245.
- Medvedev, S., Hartz, E.H., Podladchikov, Y.Y., 2008. Vertical motions of the fjord regions of central East Greenland: impact of glacial erosion, deposition, and isostasy. *Geology* 36 (7), 539–542.
- Medvedev, S., Souche, A., Hartz, E.H., 2013. Influence of ice sheet and glacial erosion on passive margins of Greenland. *Geomorphology* 193, 36–46.
- Morlighem, M., Williams, C.N., Rignot, E., An, L., Arndt, J.E., Bamber, J.L., Catania, G., Chauché, N., Dowdeswell, J.A., Dorschel, B., Fenty, I., 2017. BedMachine v3: complete bed topography and ocean bathymetry mapping of Greenland from multibeam echo sounding combined with mass conservation. *Geophys. Res. Lett.* 44 (21), 11–51.
- Nielsen, S.B., Gallagher, K., Leighton, C., Balling, N., Svenningsen, L., Jacobsen, B.H., Thomsen, E., Nielsen, O.B., Heilmann-Clausen, C., Egholm, D.L., Summerfield, M.A., 2009. The evolution of western Scandinavian topography: a review of Neogene uplift versus the ICE (isostasy–climate–erosion) hypothesis. *J. Geodyn.* 47 (2–3), 72–95.
- Pedersen, G.K., Nøhr-Hansen, H., Haggart, J.W., 2014. Sedimentary successions and palynoevent stratigraphy from the non-marine Lower Cretaceous to the marine Upper Cretaceous of the Nuussuaq Basin, West Greenland. *Bull. Can. Petrol. Geol.* 62 (4), 261–288.
- Pedersen, V.K., Huismans, R.S., Moucha, R., 2016. Isostatic and dynamic support of high topography on a North Atlantic passive margin. *Earth Planet. Sci. Lett.* 446, 1–9.
- Piasecki, S., Larsen, L.M., Pedersen, A.K., Pedersen, G.K., 1992. Palynostratigraphy of the lower Tertiary volcanics and marine clastic sediments in the southern part of the West Greenland Basin: implications for the timing and duration of the volcanism. *Rapport Gronlands Geologiske Under-søgelse* 154, 13–31.
- Pinet, N., Lavoie, D., Dietrich, J., Hu, K., Keating, P., 2013. Architecture and subsidence history of the intracratonic Hudson Bay Basin, northern Canada. *Earth Sci. Rev.* 125, 1–23.
- Recanati, A., Gautheron, C., Barbarand, J., Misseand, Y., Pinna-Jamme, R., Tassan-Got, L., Carter, A., Douville, É., Bordier, L., Pagel, M., Gallagher, K., 2017. Helium trapping in apatite damage: Insights from (U–Th–Sm)/He dating of different granitoid lithologies. *Chem. Geol.* 470, 116–131.
- Redfield, T.F., 2010. On apatite fission track dating and the Tertiary evolution of West Greenland topography. *J. Geol. Soc.* 167 (2), 261–271.
- Redfield, T.F., Osmundsen, P.T., 2014. Some remarks on the earthquakes of Fennoscandia: a conceptual seismological model drawn from the perspective of hyperextension. *Nor. J. Geol.* 94 (4), 233–262.
- Redfield, T.F., Osmundsen, P.T., Hendriks, B.W.H., 2005. The role of fault reactivation and growth in the uplift of western Fennoscandia. *J. Geol. Soc.* 162 (6), 1013–1030.
- Reiners, P.W., Farley, K.A., 2001. Influence of crystal size on apatite (U–Th)/He thermochronology: an example from the Bighorn Mountains, Wyoming. *Earth Planet. Sci. Lett.* 188 (3–4), 413–420.
- Riis, F., 1996. Quantification of Cenozoic vertical movements of Scandinavia by correlation of morphological surfaces with offshore data. *Glob. Planet. Chang.* 12 (1–4), 331–357.
- Roberts, D.H., Rea, B.R., Lane, T.P., Schnabel, C., Rodés, A., 2013. New constraints on Greenland ice sheet dynamics during the last glacial cycle: evidence from the Uummannaq ice stream system. *J. Geophys. Res. Earth Surf.* 118 (2), 519–541.
- Rohrman, M., Andriessen, P., van der Beek, P., 1996. The relationship between basin and margin thermal evolution assessed by fission track thermochronology: an application to offshore southern Norway. *Basin Res.* 8 (1), 45–63.
- Schaefer, J.M., Finkel, R.C., Balco, G., Alley, R.B., Caffee, M.W., Briner, J.P., Young, N.E., Gow, A.J., Schwartz, R., 2016. Greenland was nearly ice-free for extended periods during the Pleistocene. *Nature* 540 (7632), 252.
- Shuster, D.L., Flowers, R.M., Farley, K.A., 2006. The influence of natural radiation damage on helium diffusion kinetics in apatite. *Earth Planet. Sci. Lett.* 249 (3–4), 148–161.
- Sidgren, A.S., Page, L., Garde, A.A., 2006. New hornblende and muscovite <sup>40</sup>Ar/<sup>39</sup>Ar cooling ages in the central Rinkian fold belt, West Greenland. *Geological Survey of Denmark and Greenland Bulletin* 11, 115–123.
- Stock, J.D., Montgomery, D.R., 1999. Geologic constraints on bedrock river incision using the stream power law. *J. Geophys. Res. Solid Earth* 104 (B3), 4983–4993.
- Stockli, D.F., Farley, K.A., Dumitru, T.A., 2000. Calibration of the apatite (U–Th)/He thermochronometer on an exhumed fault block, White Mountains, California. *Geology* 28 (11), 983–986.
- St-Onge, M.R., Van Gool, J.A., Garde, A.A., Scott, D.J., 2009. Correlation of Archaean and Palaeoproterozoic units between northeastern Canada and western Greenland: constraining the pre-collisional upper plate accretionary history of the Trans-Hudson orogen. *Geol. Soc. Lond., Spec. Publ.* 318 (1), 193–235.
- Storey, M., Duncan, R.A., Pedersen, A.K., Larsen, L.M., Larsen, H.C., 1998. <sup>40</sup>Ar/<sup>39</sup>Ar geochronology of the West Greenland Tertiary volcanic province. *Earth Planet. Sci. Lett.* 160 (3), 569–586.
- Strunk, A., Knudsen, M.F., Egholm, D.L., Jansen, J.D., Levy, L.B., Jacobsen, B.H., Larsen, N.K., 2017. One million years of glaciation and denudation history in west Greenland. *Nat. Commun.* 8, 14199.
- Swift, D.A., Persano, C., Stuart, F.M., Gallagher, K., Whitham, A., 2008. A reassessment of the role of ice sheet glaciation in the long-term evolution of the East Greenland fjord region. *Geomorphology* 97 (1–2), 109–125.

- Thiede, J., Jessen, C., Knutz, P., Kuijpers, A., Mikkelsen, N., Nørgaard-Pedersen, N., Spielhagen, R.F., 2011. Million years of Greenland Ice Sheet history recorded in ocean sediments. *Polarforschung* 80 (3), 141–149.
- Vermeesch, P., Seward, D., Latkoczy, C., Wipf, M., Günther, D., Baur, H., 2007.  $\alpha$ -Emitting mineral inclusions in apatite, their effect on (U-Th)/He ages, and how to reduce it. *Geochim. Cosmochim. Acta* 71 (7), 1737–1746.
- Wildman, M., Brown, R., Watkins, R., Carter, A., Gleadow, A., Summerfield, M., 2015. Post break-up tectonic inversion across the southwestern cape of South Africa: new insights from apatite and zircon fission track thermochronometry. *Tectonophysics* 654, 30–55.
- Zeitler, P.K., Herczeg, A.L., McDougall, I., Honda, M., 1987. U-Th-He dating of apatite: a potential thermochronometer. *Geochim. Cosmochim. Acta* 51 (10), 2865–2868.
- Zeitler, P.K., Enkelmann, E., Thomas, J.B., Watson, E.B., Ancuta, L.D., Idleman, B.D., 2017. Solubility and trapping of helium in apatite. *Geochim. Cosmochim. Acta* 209, 1–8.